Relationship between microstructures and grain-scale trace element distribution in komatiite-hosted magmatic sulphide ores

Zoja Vukmanovic[1,2], Steven M. Reddy[3], Bélinda Godel[2], Stephen J. Barnes[2], Marco L. Fiorentini[1], Sarah-Jane Barnes[4], Matt R Kilburn[5]

[1]Centre for Exploration Targeting, The University of Western Australia, & ARC Centre of Excellence for Core to Crust Fluid Systems, Crawley, WA 6009, Western Australia. *zoja.vukmanovic@uwa.edu.au, marco.fiorentini@uwa.edu.au*

[2] CSIRO Earth Science and Resource Engineering, Australian Research Centre, Kensington, WA 6151, Australia. *steve.barnes@csiro.au, belinda.godel@csiro.au*

[3] ARC Centre of Excellence for Core to Crust Fluid Systems, Curtin University, Department of Applied Geology, PO Box U1987, Perth WA 6845, Australia. *s.reddy@curtin.edu.au*

[4]Département des Sciences Appliquées, Unité d'enseignement en sciences de la Terre, 555 Boulevard de l'Université, Chicoutimi, Québec, Canada, G7H 2B1. *sjbarnes@uqac.ca*

[5] Centre for Microscopy, Characterisation and Analysis, The University of Western Australia, & ARC Centre of Excellence for Core to Crust Fluid Systems, Crawley, WA 6009, Western Australia. *matt.kilburn@uwa.edu.au*

1. Introduction

Komatiites and associated magmatic nickel sulphide ores in the Archean Yilgarn Craton (Western Australia; Fig. 1) have experienced a diverse range of metamorphic conditions and deformation histories (Goscombe et al., 2009). It has been widely accepted that the key ore forming process in komatiite-hosted deposits involves assimilation of sulphidic country rocks by komatiitic magma, followed by accumulation of droplets or pools of Ni-rich immiscible sulphide liquid (Bekker et al., 2009; Fiorentini et al., 2012; Huppert and Sparks, 1985; Huppert et al., 1984; Lesher et al., 1984). Sulphide mineralogy in komatiite-hosted Ni deposits consists mostly of pyrrhotite ($Fe_{1-x}S$), pentlandite ($(Fe,Ni)_8S_9$), with minor chalcopyrite ($CuFeS_2$) and pyrite (FeS_2). Sulphide phases are commonly associated with magnetite (Fe_3O_4) and chromite ($(Fe,Mg)(Cr,Al,Fe)_2O_4$) whereas arsenides can occasionally be found in trace amounts. Depending on sulphide modal abundance, three different sulphide types can be formed: massive sulphide (>70 % vol. sulphides); matrix sulphide (30-70 % vol.) comprising a framework of olivine crystals within a continuous matrix of sulphide; and disseminated sulphide (<30 and typically 1-5 % vol.).

Typical immiscible sulphide melts associated with komatiites have high Ni and low Cu contents, and starts crystallizing as Fe-rich monosulphide solid solution (MSS) at around 1100°C (Naldrett et al., 1967). At temperatures below about 800°C, depending on the Ni tenor (Ni content in the sulphide fraction), pentlandite starts exsolving from MSS. Exsolution continues down to below 300°C as fine-grained "flame" pentlandite within pyrrhotite. Pyrite, in most cases, forms as the result of post-magmatic sulphidation or oxidation, although a small proportion may form by decomposition of S-rich MSS below 750°C depending on the metal/S ratio of the sulphide melt (Farrell and Fleet, 2002; Naldrett, 2004; Naldrett and

Kullerud, 1967; Sugaki and Kitakaze, 1998). Chalcopyrite forms from the late-crystallising Cu-rich residual liquid.

During metamorphism, the mineralogy of the ores may revert to being dominated by MSS, depending on the bulk composition and temperature (Hill, 1984; Kullerud et al., 1969; McQueen, 1979a, 1987; Naldrett et al., 1967). Marston (1984) suggested that most of the sulphide deposits around the Kambalda Dome would have been mostly homogeneous MSS during deformation. Subsequent experimental studies (Farrell and Fleet, 2002; Sugaki and Kitakaze, 1998) have extended the upper temperature at which pentlandite is potentially stable, and allow for the possibility that typical Ni-rich ores may have deformed as mixtures of multiple Ni-rich and Ni-poor sulphide phases under upper greenschist to lower amphibolite conditions. This may explain the presence of prominent pentlandite-pyrrhotite banding in some deformed Kambalda ores (Cowden and Archibald, 1987).

Groves et al. (1979) attributed a major role to metamorphism and deformation in controlling grade and tenor, suggesting that high metamorphic grade may be essential for the formation of massive ores. This contention is not widely accepted nowadays, but a diversity of opinion still exists on whether deformation and metamorphism play a significant role, and at what scale, in the modification of ore and tenors. Critical to this argument is the extent to which pentlandite redissolves in MSS and whether MSS forms a homogenous phase under metamorphic conditions. Seat et al. (2004), suggested that tenor is significantly modified as a result of a ductility contrast between Ni-rich and Ni-poor MSS: in their model, Ni-poor MSS (the weaker MSS) relocates along the shear zones causing tenor variations within the ore and destruction of primary ore textures. Deformation of sulphide has been shown to be strongly dependent on temperature, while pressure has a smaller effect on its rheology (Clark and Kelly, 1973; Kelly and Clark, 1975). With increasing temperature, pyrrhotite becomes the weakest phase compared with chalcopyrite and galena (Clark and Kelly, 1973; Cox, 1987;

Kelly and Clark, 1975). According to the deformation mechanism map proposed by Cox (1987), pyrrhotite exhibits dislocation creep at greenschist and mid-amphibolite grade metamorphic conditions. Recent electron backscatter diffraction (EBSD) studies on pyrite suggest lower temperatures of 200-260°C for the brittle – ductile transition (Barrie et al., 2009b; Barrie et al., 2011).

In a study of the komatiite-hosted Redross Ni sulphide deposit, sulphides showed evidence of dislocation creep and diffusion creep microstructures (McQueen, 1979b). This author suggested that kinking and twining of the pyrrhotite occurred at 300-550°C whereas annealing textures are recorded at higher temperatures, >500°C. Such microstructures in pyrrhotite have been associated with a large-scale remobilisation event (McQueen 1987).

Over the past 10 years, the advance of laser ablation inductively couple plasma mass spectrometry (LA-ICP-MS) has made it possible to determine the *in situ* concentration of a range of minor and trace elements in magmatic sulphide minerals. Much of this work has focussed on platinum group elements (Ballhaus and Sylvester, 2000; Barnes et al., 2008; Barnes et al., 2006; Godel and Barnes, 2008; Godel et al., 2007; Hanley, 2007; Holwell and McDonald, 2007; Huminicki et al., 2005). More recently, a wider variety of elements were included in LA-ICP-MS analysis, such as Se, Bi, Te and As (Dare et al., 2010; 2011; Godel et al., 2012; Hanley, 2007; Piña et al., 2013; 2012). Laser ablation ICP-MS element maps have revealed the presence of trace element zonation in pyrite (Dare et al., 2011; Piña et al., 2013). Nano-scale secondary ion mass spectrometry (NanoSIMS) has also been used to map trace element distributions at the sub-micron scale in sulphide minerals, particularly in Au-bearing Carlin-type deposits (Barker et al., 2009). However, the role of deformation and metamorphism on trace element distribution and concentration in magmatic sulphides has not yet been considered.

Studies integrating microstructural and mineral chemical analysis of non-sulphide minerals show evidence for strong dependence between the microstructures and trace element concentrations. Such observations have been documented in zircons (Reddy et al., 2007; Reddy et al., 2006; Timms et al., 2006; Timms et al., 2012), garnet (Keller et al., 2006), feldspars (Mark et al., 2008; Reddy et al., 2001), olivine (Plümper et al., 2012) and tourmaline (Büttner and Kasemann, 2007). These studies imply that grain-scale trace element heterogeneities may be influenced by deformation as much as by original crystal growth processes. This possibility has not as yet been considered for magmatic sulphides. This study is the first to combine quantitative microstructural – geochemical analyses of nickel sulphides using EBSD, LA-ICP-MS and NanoSIMS. The aims are to quantify the deformation of the main sulphide phases (pyrrhotite, pentlandite and to a lesser extent pyrite) within a range of deposits that have experienced different metamorphic and deformational histories, and to establish the relationship between the microstructures and variability in grain-scale trace element mineral composition under the different conditions represented by these deposits.

2. Geological settings

The sample material has been chosen from massive sulphide ore shoots from three different deposits from the Archean Yilgarn craton of Western Australia: 1) Silver Swan, 2) Perseverance and 3) Flying Fox; (Fig. 1).

2.1. Silver Swan

The Silver Swan ore shoot (Dowling et al., 2004) is the larger of two Type 1 deposits located within the Black Swan komatiite complex 70km NE of Kalgoorlie (Fig. 2a, b). Silver Swan is among the highest grade Ni sulphide deposits of any type in the world, with a pre-mining resource of 400kt at 9.4% Ni and Ni tenors averaging close to 16% (Dowling et al., 2004). Nickel sulphide ores at the Black Swan locality comprise a number of distinct

massive (Silver Swan and Gosling) and disseminated (Cygnet and Black Swan) orebodies hosted within a bimodal association of dacitic and komatiitic volcanic rocks that belongs to the Boorara Domain of the Kalgoorlie Terrane in the eastern Yilgarn craton (Barnes, 2004; Cassidy et al., 2006). The deposit and its host rocks occupy the steeply dipping flank of a regional antiform, but display very little penetrative deformation with primary stratigraphic relationships being well preserved (Hill et al., 2004). The assemblage experienced lower greenschist facies metamorphism in the presence of CO_2 rich fluids and reached peak metamorphic temperatures of approximately 300-350°C, based on the presence of talc-carbonate-chlorite-quartz and millerite-pentlandite-pyrite assemblages (Barnes et al., 2009; Hill et al., 2004).

2.2. Perseverance

The Perseverance deposit (formerly known as Agnew) is one of the world's largest komatiite hosted nickel sulphide deposit and is located in the ~ 2.7Ga Agnew-Wiluna greenstone belt (Barnes, 2006; Barnes et al., 2011; Barnes et al., 1988); (Fig. 2c, d). Stratigraphy at Perseverance comprises from bottom to top a sequence of mainly dacitic volcano-sedimentary rocks, now metamorphosed to gneisses; the komatiitic Perseverance Ultramafic Complex; intermediate (volcano–) sedimentary hanging wall units to the Perseverance ultramafic complex; and the East Perseverance komatiite. The main deposit is hosted by the Perseverance Ultramafic Complex, a large lenticular body of mostly coarse grained adcumulate dunite 2.5 km wide and about 700m thick. The deposit comprises a large tonnage of matrix ores, associated with variably tectonised massive ores with a combined pre-mining resource of of 31,300 kt at 5.9% Ni (Barnes, 2006), at tenors averaging about 9% Ni in massive and matrix ore. The area has undergone a high-strain, polyphase deformation history at low- to mid-amphibolite facies metamorphic conditions (Duuring et al., 2010). Gole et al. (1987) used garnet-biotite thermometry to constrain the metamorphic temperature peak at

535-560°C with pressures estimated at 3 kbar. A number of discrete massive sulphide shoots exist (Duuring et al., 2010), including the 1A massive sulphide ore shoot and basal contact massive sulphide (Fig. 2c, d). The Perseverance sample comes from the basal contact massive sulphide (Fig. 2c, d).

2.3. Flying Fox

The Flying Fox deposit occurs within the 2.9 Ga Forrestania greenstone belt, which is the southward extension of the Southern Cross greenstone belt (Perring et al., 1996; Porter and McKay, 1981); (Fig 2e). The pre-mining total resource at Flying Fox stood at 315kt at 1.7% Ni in 2006 (Barnes, 2006) with average Ni tenor about 7% (Collins et al., 2012a). Peak metamorphism for the Forrestania greenstone belt has been estimated by Porter and McKay (1981) at 655°C and 4 kbar on the base of mineral assemblages (quartz + biotite + sillimanite ± garnet and quartz + biotite + sillimanite ± andalusite ±plagioclase) present in country-rock pelitic schists. Peak metamorphism has been extensively overprinted by retrograde hydrothermal alteration, resulting in serpentinisation of metamorphic olivine, and development of overprinting porphyroblastic pyrite in the ores (Perring et al., 1995). Five regional deformation events and four hydrothermal events have been recognised, one of these being associated with injection of sub-horizontal granitic sheets cross cutting the orebody (Collins et al., 2012b). Ore bodies have been sheared and dismembered in up to 11 discrete ore shoots. Massive ores show variable degrees of mobilisation, widespread development of breccia textures, and in some places incorporation into the late intruding granite sills. Collins et al. (2012b) concluded that Ni sulphide orebodies were mechanically relocated along the footwall on a scale of tens of metres. The Flying Fox sample investigated in this study is from the T1 ore body and is closely associated with hydrothermal quartz veining and pervasive retrograde alteration related to the granite sheets (Fig. 2e, f).

3. Analytical Methodology

The microstructural characterisation of sulphide minerals was undertaken by reflected light optical microscopy and EBSD. Platinum group elements and other trace elements in sulphides were analysed with LA-ICP-MS, and the Flying Fox sample was also mapped using NanoSIMS.

3.1. Electron Backscatter Diffraction Analysis (EBSD)

Electron backscatter diffraction is a technique whereby crystal lattice orientation can be measured and mapped at sub-micron scale. Samples were prepared according to usual EBSD protocols (e.g. (Prior et al., 1999; Reddy et al., 2007)) and were polished with a broad ion beam polisher. The second step was found to be essential in order to obtain good crystallographic patterns for the pentlandite.

Data were collected using a Zeiss Evo 40XVP SEM at Curtin University (Perth, Western Australia). All EBSD data have collected and processed using Oxford Instruments software package CHANNEL 5.10 (for more details see supplementary table 1). The typical error for EBSD lattice orientation analysis on this instrument is less than 0.5°.

Orientation data are plotted in a series of maps and lower-hemisphere, equal-area stereographic projections (see Reddy et al. (2007) for details). Inverse pole figure maps provide information on crystal orientation relative to a particular user-defined sample direction (X, Y or Z). Cumulative misorientation maps show relative differences in lattice orientation with respect to an arbitrary user-defined reference point within the grain. Grain boundary and misorientation axis maps display the presence of the grain boundaries in the sample and also the orientation of misorientation axes along the grain boundaries relative to the sample reference frame. Local misorientation maps were plotted to show the relative

crystallographic misorientation within the grain. In all studied samples, EBSD successfully indexed pyrrhotite as a hexagonal crystal symmetry.

3.1.1 Misorientation boundary analysis

Electron backscatter diffraction data is used to characterise microstructures in the crystals. Formation of the low angle boundaries can be part of the recovery process where dislocations in the crystal lattice migrate to form planar arrays of dislocations (Passchier and Trouw, 2005; Trimby et al., 1998) or they can also be formed during mineral growth (Timms et al., 2009). The two main types of the low angle boundaries are 1) tilt and 2) twist boundaries (Fig. 3). The crystallographic expression of the tilt and twist low angle boundaries is defined by the relationship between the boundary and the misorientation axis (Lloyd (2004); Lloyd and Freeman (1994); Reddy et al. (2007); Fig. 3). In most cases, to determine if the boundary is tilt or twist type, two sections to reconstruct 3D orientation of the particular boundary are needed (Barrie et al., 2009a; Reddy et al., 2007).

3.2. Laser ablation - Inductively coupled plasma mass spectrometry

In situ chalcophile and PGE concentrations within the sulphides were determined by LA-ICP-MS at LabMaTer University of Quebec at Chicoutimi (UQAC), Canada using an Excimer (193nm) Resolution M-50 laser (Resonics) attached to an Agilent 7700x ICP-MS. Data were collected for the following isotopes: ^{29}Si, ^{33}S, ^{34}S, ^{57}Fe, ^{59}Co,^{60}Ni, ^{61}Ni, ^{63}Cu, ^{65}Cu, ^{66}Zn, ^{68}Zn, ^{75}As, ^{77}Se, ^{82}Se, ^{95}Mo, ^{99}Ru, ^{100}Ru, ^{101}Ru, ^{102}Ru, ^{103}Rh, ^{105}Pd, ^{106}Pd, ^{107}Ag, ^{108}Pd, ^{109}Ag, ^{111}Cd, ^{118}Sn, ^{121}Sb, ^{125}Te, ^{126}Te, ^{128}Te, ^{185}Re, ^{189}Os, ^{190}Os, ^{193}Ir, ^{194}Pt, ^{195}Pt, ^{197}Au, ^{208}Pb and ^{209}Bi. The analyses were carried out in raster mode by using a laser beam size of 42 μm and speed of 5 μm/s. In addition, semi-quantitative trace element concentration maps of selected areas were carried out with a beam size of 10 μm and a speed of 20 μm/s. A cleaning of the surface by the laser was performed before each new profile was collected to avoid artefacts

due to the deposition of materials during previous ablations. Trace element concentrations were calculated along the profile by subtracting the gas background from the signals of each of the analysed isotopes using IOLITE software (Hellstrom et al., 2008). ^{34}S was used as an internal standard to calculate the concentration of trace elements in the sulphides with stoichiometric values used for each different sulphide. The calibration was carried out using certified reference materials: Laflamme –P0727 and, MASS-1 (previously referred to as PS-1). Quality control was monitored by analysing in-house reference materials (JB-MSS-5 and NiS) previously used in numerous studies (Godel et al., 2012; Piña et al., 2013; Piña et al., 2012). Reference materials and samples were placed in the sample chamber together. Reference materials were analyzed at the beginning and end of the sessions and between each sample. Element concentrations were corrected for argide interferences as follows: (i) ^{101}Ru was corrected for $^{61}Ni^{40}Ar$ interferences; (ii) ^{103}Rh was corrected for $^{63}Cu^{40}Ar$; ^{105}Pd was corrected for $^{65}Cu^{40}Ar$. A number of other interferences on ^{106}Pd and ^{108}Pd (^{106}Cd and ^{108}Cd overlap, $^{66}Zn^{40}Ar$ and $^{68}Zn^{40}Ar$) were considered but their effects in our samples are less than the detection limits. Results for the reference materials, quality control monitors and standard references are presented in supplementary table 2.

3.3. Nano-scale secondary ion mass spectrometry (NanoSIMS)

Nano-scale secondary ion mass spectrometry (NanoSIMS) is a high sensitivity and high resolution imaging mass spectrometry technique, allowing elemental and isotopic images to be acquired at sub-micron scales. High-resolution secondary ion imaging was performed using a Cameca NanoSIMS 50 at The University of Western Australia (UWA). Positive secondary ions (^{54}Fe, ^{58}Ni, ^{59}Co, ^{63}Cu, ^{107}Ag, ^{133}Cs, ^{208}Pb in various combinations) were sputtered from the sample surface using a ~600nm O^- primary beam, with a beam current of 24 pA. Negative secondary ions (^{34}S, ^{78}Se, $^{75}As^{32}S$, ^{107}Ag, ^{109}Ag ^{130}Te, ^{197}Au, ^{209}Bi in various combinations) were sputtered using a ~100nm Cs^+ primary ion beam, with a beam current of

3 pA. Peak positions were calibrated using pure metal standards and Wood's alloy ($Bi_{50}Cd_{12.5}Pb_{25}Sn_{12.5}$).

Regions-of-interest were pre-sputtered to $2x10^{17}$ ions/cm^2 prior to imaging. Images were acquired from 25 x 25 μm areas (identified by optical microscopy) at a resolution of 256 x 256 pixels. The dwell time was 60ms/pixel. Images were corrected for 44ns detector dead time and processed using the Open-MIMS plugin for ImageJ. Line scans for the positive secondary ions were also obtained with a spot size of 600 nm.

3.4. Image analysis

Greyscale local misorientation maps were processed using image analysis software (ImageJ 1.46) to compare local misorientation values, from EBSD data, against variation in trace element concentration. The areas of the laser ablation profiles have been cropped from the local misorientation maps and have been processed with MatLab™ to obtain numerical values of local misorientation along each profile. The two sets of data have been plotted together to show the relationship between lattice distortion and trace element variation.

4. Petrography

4.1. Silver Swan

Sulphide phases in the Silver Swan massive sulphide sample include pyrrhotite (55 modal %), pentlandite (30%), pyrite (10%) and trace arsenopyrite. The sample contains aggregates of calcite and chlorite intergrown with pentlandite crystals, and also small veins composed of fine grained carbonates and minor chlorites. Fine carbonate veins containing pyrrhotite inclusions are often associated with fine-grained lobate arsenopyrite (~100 μm; Fig. 4a). Pyrrhotite has euhedral habit with grains up to 1mm long (Fig. 4a, b) decreasing to <50μm where found within the veinlets. Pyrrhotite commonly contains inclusions of euhedral pyrite

(Fig. 4a, b) and to a lesser extent pentlandite flame exsolution, along with rare arsenopyrite inclusions a few microns in size.

In this particular thin section, globular pentlandite (>200μm) is mostly associated with an aggregate of carbonate, chlorite and quartz that covers around 25% of the thin section. Pentlandite is also present as ribbon-like aggregates between the pyrrhotite grains (<200μm). Pyrite is present as euhedral prismatic grains (~150μm) and as well as ribbon-like lenses inside the globular pentlandite (300μm).

4.2. Perseverance

The Perseverance massive sulphide sample contains pyrrhotite (50% modal), pentlandite (35%), chalcopyrite (3%), pyrite (5%), arsenopyrite (1%), carbonates and anthophyllite (~5%) and magnetite (1%). Pyrrhotite grains are equant with relatively uniform grain size (~500μm); in general their size is smaller (~20μm) when surrounded by other sulphide phases. In crossed polarized reflected light, pyrrhotite shows strongly kinked microstructures (Fig. 4d). In the thin section, pyrrhotite locally shows significant reduction in size (~50 μm). Pentlandite is present in thin section both as globular (~300 μm) and flame exsolutions. Flame exsolutions are often associated with kinked macrostructures or grain boundaries in pyrrhotite (Fig. 4c, d). Pentlandite commonly contains or adjoins anthophyllite. Pyrite is euhedral, varies from 100μm to <30μm in size and forms ribbon-like interstitial grains between pyrrhotite grains. Chalcopyrite is commonly associated with silicates or is observed along with pyrite. Arsenopyrite forms subhedral grains up to 150μm in size and shows evidence of zonation under crossed polarized light. Apart from sulphide phases, carbonates are ~300 μm in size whereas anthophyllites are ~100 μm and show euhedral prismatic habit.

4.3. Flying Fox

The sample from Flying Fox consist of a band of massive sulphide (40%) that is between amphibole rich material (50%) and a quartz vein (Fig. 2e, f). Sulphide mineralogy consists of pyrrhotite (45% modal), pyrite (35%), pentlandite (15%) and chalcopyrite (2%). The oxide phase in the sample is magnetite (~3%). Pyrrhotite grains are very large (>1cm) and contain multiple sets of wedge-shaped deformation twins extending across entire grains (Fig. 4e, f). The large pyrrhotite grain contains numerous pentlandite exsolution lamellae and fine globular pentlandite (~100μm in diameter). Pyrite in the sample has euhedral habit (2.5cm in diameter) and is strongly fractured. Pyrite contains numerous magnetite inclusions and fracture-filling chalcopyrite. Pentlandite in this sample is present as globular, ribbon-like, and flame exsolution types (Fig. 4e, f). Globular pentlandite (mm in size) is typically present at the contact with pyrite or with the quartz vein. Pentlandite observed within pyrrhotite matrix shows slightly finer grain size (400-100μm). Ribbon-like pentlandite is present along the grain boundaries of pyrrhotite (~200-300μm) (Fig. 4e, f).

Amphiboles have euhedral prismatic habits and show very well developed shape-preferred orientation (Fig. 4e, f). They are a few mm long and often contain sulphides along their cleavage planes. Quartz grains are very coarse (few cm in size; Fig. 4e, f) and contain numerous fluid inclusions. Iron oxides are often present at the grain boundaries between the quartz vein, massive sulphide and the ultramafics.

5. Intragrain microstructural analyses of Ni sulphides

5.1. Silver Swan

Electron backscatter diffraction data of pyrrhotite from Silver Swan shows the presence of numerous low angle boundaries of 2-15° (Fig. 5). Low angle boundaries are mainly focused around a pyrite grain with high angle boundaries (>15°) being intra-connected with lower

angle (<15°) boundaries (Fig. 5a). The cumulative misorientation map of the pyrrhotite grain shows a total misorientation in the grain to be 35° whereas in the pyrite, cumulative misorientation does not exceed 4° (Fig. 5c, d). The misorientation axes map reveals that most of the low angle boundaries indicate misorientation axes parallel to the Y and Z direction of the sample reference frame, whereas rare low angle boundaries, such as the low angle boundary at the top of laser liner SS 2, misorientation axes parallel to the X direction (red misorientation axis; Fig. 5b).

Crystallographic data of the pyrrhotite is strongly dispersed with misorientation axes showing rotation around a number of different axes (Fig. 5e). The stereographic projection shows an array of rotation axes in the basal planes with varying contributions from crystallographic directions <10-10> and <11-20>, and a smaller cluster that corresponds to {0001} axis (Fig. 5e (2)).

The laser ablation line SS 2 traverses three low angle boundaries before crossing the phase boundary between pyrrhotite and pyrite (Fig 5a, c). Rotation axes along low angle boundary "**1**" display strongly dispersed cluster of <10° (Fig. 5f); however, they show good correlation with dispersion axis (0001); (Fig 5f). Since the crystallographic axis {0001} is contained in the boundary wall, low angle boundary "***1***" is consistent with a tilt wall formed from the dislocations of a prism slip system {11-20}<10-10> (Fig. 5f).

The laser ablation line SS 1 transects one low angle boundary (<15°) and two high angle boundaries (>15°); (Fig. 5a, g). The curved low angle boundary "**2**" is analysed in two steps: "**2a"** (N-S orientation) of predominantly 10-15° of rotation and "**2b"** of <10° of rotation. The N-S low angle boundary marked as "**2a"** displays a well developed cluster of 10-15° rotation axes that mildly correlate with dispersion axis <11-20> (Fig. 5g (2a)). Reconstruction of the slip system by using dispersion axis corresponds to a basal slips system {0001}<10-10>. The curved part of the low angle boundary "**2**", "**2b**" contains rotation axes that express more than

15° of dispersion. The relationship between rotation axis and the trace of the boundary implies that this low angle boundary can be result of either tilt or twist of the crystal. If the **2b** is the tilt boundary, the rotation axes are correlated poorly with dispersion axis <10-10>, as a result of multiple slip systems operating along boundary "**2b"** (Fig. 5g (2b)).

5.2. Perseverance

The inverse pole figure map indicates that pyrrhotite grains show strong crystallographic preferred orientation in the sample reference frame, with one grain having different orientation than its neighbouring grains (grain 4, Fig. 6a). Pyrrhotite grains contain sub-parallel sets of low angle boundaries (Fig. 6a, b (1-3)). These boundaries within four different pyrrhotite grains contain multiple rotation axes that either correspond with two lower symmetry axes, <10-10> and <11-20>, or are the product of mixing of the two (Fig. 6c, d (1-3)). In grain 4, which is oriented differently than its neighbouring grains, the rotation axis is also different to the surrounding grains, corresponding to the c axis, (0001) with slight mixing with <10-10> and/or <11-20>; (Fig 6a-d, grain 4).

Rotation axes in the grain 2 display the strongest cluster corresponding to the mix between <10-10> and <11-20> axes (Fig. 6a, b, c (2)). Other clusters correlate to individual axes (<10-10> or <11-20>). When the boundaries in the grain 2 are looked at in more detail, the imperfect fit to a slip system is observed (Fig. 6e, f). Electron back scatter data of the area around boundary "**1**" shows ~10° of dispersion around <10-10> axis. The dispersion axis shows good correlation with well clustered rotation axes of 10-15°, implying the formation of the boundary as a response to the tilting of the crystal lattice along the {0001}<11-20> slip system (Fig. 6e). Dispersion of the crystal lattice along the low angle boundary "**2**" is ~10° around the <11-20> axis (Fig. 6f). A well developed cluster of rotation axes along the low angle boundary "**2**" does not correspond to any lower symmetry axis, but may represent

mixing between <10-10> and <11-20> and a minor contribution of {0001} axes. Such complex lattice rotation suggests multiple slip systems operating around the boundary "**2**".

Pentlandite grains within aggregates are separated by high-angle grain boundaries (Fig 6b (5)) and shows of maximum cumulative misorientation of 6°. The pentlandite rotation axis shows good correlation with a dispersion axis corresponding to (110); (Fig. 6c, d (5)). In the case of the low angle boundary in pentlandite, denoted as "**3**", pole figures show 6° rotation around a dispersion axis that corresponds to the <110> axis (Fig. 6g). However, rotation axes have up to 15° of dispersion, preventing accurate slip system determination.

5.3. Flying Fox

The inverse pole figure map displays different crystallographic orientations for twin and the host relative to the X direction of the sample (Fig. 7a, d). The common crystallographic axis <10-10> of the twin and the host corresponding to a rotation angle of 85° (Fig. 7d (1, 2), e).

The pyrrhotite pole figure data shows that *c* axes (0001) of the twin and the host are 85° apart (Fig. 7d). The common axis <10-10> for the both host and the twin grain is a twin rotation axis around which the {0001} axis rotated by ~ 85° <10-10>; (Fig. 7d (3), e). This rotation axis is contained along the trace of the twin boundary which also belongs to the twin plane (Fig. 7f, g). Hence, the pole to the plane that contains the trace of the twin boundary and the rotation axis is the pole to the twin plane, {11-21} (Fig 7f, g). The crystallographic relationship implies that the deformation twin is a pyramidal twin {11-21}(10-10).

Rotation axes in pyrrhotite with less than 15° of rotation display an array of orientation between <11-20> and <10-10> axes (Fig. 7d (2), f). The maximum misorientation within individual pyrrhotite grains (twin and the host) is around 15° (Fig. 7b, c). Low angle boundaries (<15°) are present throughout the map but commonly are related to the presence of the pentlandite exsolutions or recrystallysed pyrrhotite grains (Fig. 7a, b).

Pentlandite grains within aggregates are separated by high angle grain boundaries and show only weak evidence of crystal plasticity (Fig 7h). A single pentlandite grain (Fig. 7h (2)) shows very weak dispersion of its crystallographic orientation. The rotation axis do not correspond to any of the low symmetry axes but it is a result of mixing of multiple axes (Fig. 7h (3)).

6. Trace element and platinum group element concentrations in sulphide phases

Laser ablation ICP-MS data are shown for each element and phase as box and whisker plots (Fig. 8). The extreme high values can be due to the presence of micro-inclusions rather than high concentration as solid solution in the lattice. Concentrations of most trace elements are generally highest in pyrite, followed by pentlandite, with lowest values in pyrrhotite (Fig. 8). Values for cobalt in pyrrhotite show large variations between the deposits, with ~90 ppm on average in Silver Swan, 120 ppm in Perseverance and ~ 60 ppm in Flying Fox (Fig. 8b). Variations in Co are also present in other sulphide phases from the three deposits (Fig. 8b). Two other elements, Te and As, display large variations within a single phase from a single deposit, particularly Te in pentlandite from Perseverance, and As in pyrite from Flying Fox (Fig. 8c, d). Values for Pb, in all three deposits, are relatively uniform with pyrite having the highest Pb of all three phases (~15ppm in Black Swan) whereas normal maximum Pb concentrations in pyrrhotite (excluding Pb inclusions) are between 1-3ppm in all three deposits (Fig. 8a). The concentration of trace and Pd and Au in the three main sulphide phases is similar in all three deposits with occasional excursions (Fig. 8g, h). Palladium values are the highest in Perseverance sulphides (~30ppm in pentlandite) and show order-of-magnitude variations within both pyrrhotite and pentlandite (Fig. 8g).

Laser ablation profiles have been obtained in all three samples. Trace element profiles often display significantly higher values than general profile trend and such values will be considered as noise.

6.1. Silver Swan laser profiles

For Pb and Ag (and in less extent Bi), LA-ICP-MS profiles in the Silver Swan sample show multiple peaks along the profiles, whereas profiles for As are relatively flat (Fig. 9a, e). Cobalt shows a peaked profile where grains contain pentlandite exsolution, but no peaks in the absence of exsolution lamellae (Fig. 9a, e). Platinum group elements are not shown along the profiles as all values fell below the detection limits (Table 1). The peaks of Pb, Ag and, to a lesser extent Bi, are present along the laser profiles regardless of the presence of pentlandite exsolution. Along the line SS1, the largest absolute variation is expressed in Pb concentration, which increases up to 10ppm for the peak values from background values of <1ppm (Fig. 9a). Bismuth shows erratic element profiles, unlike Ag which displays weakly developed peaks, resembling the Pb peaks (Fig 9b- d).

At around 500μm of the profile length of the SS2, the laser profile transverses a pentlandite exsolution between pyrrhotite and pyrite. The concentrations of the trace elements (Pb, Co, Bi and Ag) at this boundary are higher for most of the elements than anywhere else in the same pyrrhotite or pyrite grain (Fig 9e-h).

6.2. Perseverance laser profiles

Element profile “Percy 1” displays variations in Co, Ag, Pb and Bi, whereas As shows, as in the case of Silver Swan, relatively flat concentration profiles (Fig. 10a-d). Cobalt has peak values associated with pentlandite exsolution (i.e. at 100 μm length of the Percy 1; Fig. 10a-d)). The concentration along the pentlandite exsolution is more than an order of magnitude higher than in the pyrrhotite matrix for most of the elements (Fig. 9a-d). A peak at 250μm,

not related to pentlandite exsolution, displays an order of magnitude increase for Pb, Bi and Ag over their background values (Fig 10a-c). Laser ablation line "Percy 2", which crosses two low angle boundaries in the pentlandite grain, shows mild increase in Ag, Pb and Bi that corresponds with the position of one of the low angle boundaries (Fig 6a, b; Fig 10f-e).

6.3. Flying Fox laser profiles and elemental maps

Two LA-ICP-MS profiles FF1 and FF2 in the Flying Fox sample are respectively parallel to and normal to twin boundaries (Fig. 7a). Neither line traversed any pentlandite exsolution. As in case of Silver Swan and Perseverance samples, PGE concentrations are below the detection limits and are not shown. Line FF1 displays very smooth flat profiles for most of the trace elements (Fig. 11b-d) and noisy profiles for As and Co (Fig11a). Unlike line FF 1, along the line FF 2, Pb, Bi and Ag have well defined peaks at 100 and ~250μm along the profile (Fig. 11f-h). Peak values for Pb are up to 5ppm whereas background values are <1ppm (Fig.11g).

A laser ablation ICP-MS element map was made across the continuation of the same deformation twins that are documented in the EBSD map (Fig. 7 and Fig. 12a). The largest "hot spot" in all of the elements (Co, Cu, Ag, Pb and Bi; Fig. 12b-e), corresponds to pentlandite flame exsolution. Apart from larger pentlandite exsolutions (~ 40μm), Co shows few more fine hot spots (~10 μm) (Fig. 12b), which are likely due to the presence of the pentlandite exsolution beneath the surface of the section but within the ~5-10μm deep ablation volume. Lead, Bi and Ag display increased concentrations along linear features that are not related to the pentlandite exsolutions (Fig. 12c, d, e). Lead abundance in pentlandite exsolution is about 6 ppm, along the linear features it reaches around 3 ppm and in the pyrrhotite matrix the values are less than 2 ppm (same as for the Bi); (Fig. 12d, e). Rare higher values (~3 ppm) are also present as fine spots that could be caused by noise or depth

effects (Fig. 12d, e). Unlike the other trace elements, PGE do not show strong variations in sulphides (apart from Pd in pentlandite exsolution) and are not presented here.

NanoSIMS was also used to image trace elements along an adjacent deformation twin in the Flying Fox sample, with a resolution of about 600nm. Although a number of trace elements were detectable in the matrix, only Pb was clearly concentrated along the twin boundaries (Fig 12f-i). The Pb signal along the *f-g* region reflects the linear geometry of the twin boundary, whereas the *h-i* region covers an intersection of the two deformation twins, revealing the complex relationship of the two cross-cutting twins (Fig. 12f-i). Line scans revealed as much as an order of magnitude increase in the Pb signal at the twin boundary compared to the background in the matrix. The Ag and Bi signals were too low to be seen in the ion images, although the line scans suggested a possible slight increase in the Ag. As NanoSIMS suffers from complex matrix effects, the detection limits are difficult to determine, and quantification is currently not possible.

7. Intragrain microstructures and trace element variations in Ni sulphides under different geological settings

Variation in trace element chemistry is shown together with matching misorientation profiles along the ablated areas (Fig. 9, 10, 11). The data indicate that trace elements fall into two groups displaying distinctly different behaviour. Lead, Bi and Ag show distinct peaks related to the presence of high and low angle boundaries, whereas elements such as Co and As do not show such a relationship.

In the Silver Swan sample, element peaks for Pb, Bi and Ag along laser line SS 1 show good correlation with one low angle (10-15°) boundary and two high angle boundaries (>15°), respectively (Fig. 5, 9a -d). The two high angle boundaries show a higher increase in Pb than

along the 10-15° boundary: Pb reaches around 10 ppm along high angle boundaries and around 3 ppm at boundary "**2**" (Fig. 9e).

Laser ablation profiles across pyrrhotite grains from the Perseverance sample express similar patterns as shown in the Silver Swan sample (Fig. 9, 10a-d). Major increases in Pb and, to a lesser extent, Bi and Ag along the Percy 1 laser ablation line correspond to a low angle boundary of 10-15°: Pb along boundary "**1**" is up to 10 ppm relative to background values of ≥1 ppm (Fig. 10a-d). The pentlandite grain that is only mildly deformed, containing solely 2° low angle boundaries, shows relatively homogenous element concentrations with mild peak along one of the low angle boundaries (Fig. 10f-e).

The sample from Flying Fox, representing the highest metamorphic grade and highest strain of the samples studied, contains a unique microstructure in pyrrhotite: deformation twins (Fig. 7). The spatial relationship between the deformation twin microstructure and trace element concentrations is clearly evident in both LA-ICP-MS profiles and LA-ICP-MS and NanoSims trace element maps (Fig. 11, 12). Line FF 2 traverses both twin boundaries (Fig 7, 11), and shows almost an order of magnitude higher concentrations of Pb, Bi and Ag corresponding to the twin boundaries (Fig. 11f, e). It is important to notice that the laser ablation profile along line FF 2 does not traverse any pentlandite exsolutions, but the increase in concentration is solely related to the presence of the twin boundaries. Element maps also confirm that increased concentrations of Pb, Bi and Ag are manifest as linear features that correspond to observed twin boundaries, which in the case of Pb is corroborated by high-resolution NanoSIMS imaging (Fig. 12d-g).

In samples from greenschist and mid amphibolite facies (Silver Swan and Perseverance deposits), pyrrhotite low angle boundaries are mostly formed by tilting of the crystal lattice along one (or a mix of two or more) of the low symmetry axes supporting evidence of crystal plasticity. The difference between these two samples is in the way the low angle boundaries

are manifest. However, in both cases two main slip systems are documented: basal and prism (Fig. 5, 6). Silver Swan pyrrhotite contains numerous low angle boundaries that are located around the stronger phase, pyrite (Fig. 5), whereas pyrrhotite from higher metamorphic grade (the Perseverance sample) develops parallel low angle boundaries with a dominant basal slip system (Fig. 6). Limited low angle boundary development in the Silver Swan sample could be due to the lower strain environment, unlike the high-strain massive sulphide from Perseverance.

The highest concentration factor for each of Ag, Pb and Bi is present along high angle boundaries whereas the concentration factor for As is close to one (Fig. 13). In the Silver Swan sample, Pb and Bi show the highest ratios (along high angle boundaries) coincident with low angle boundaries of 10-15° around the mixed rotation axis, (Fig. 13c, d), whereas Ag shows the highest ratio along low angle boundaries of 10-15° around the <10-10> axis (Fig. 13a). In Perseverance pyrrhotite, Ag, Pb and Bi profiles show high concentration factors along the low angle boundary of 10-15° around a mixed rotation axis (Fig. 13f, g, h). As in the case of the high angle boundary, As ratios along the low angle boundaries in both Silver Swan and Perseverance pyrrhotite are close to one (Fig. 13a, e). In these two samples, concentration factors broadly decrease with decreasing boundary hierarchy, showing highest concentration factors for the higher angle boundaries (>15° and 10-15°) and lowest for the very low angle boundaries (<10°) (Fig 13b-d, f-h). Similarity between the two samples from lower greenschist and mid-amphibolite facies suggest the lack of temperature dependence on the concentration factors and observed microstructures.

In the highest metamorphic grade sample, from Flying Fox, the highest concentration factors for Pb and Bi are at high angle boundaries, and the second highest at a twin boundary (Fig. 13b-d). The arsenic concentration factor is very close to one or below one (Fig. 13a). The absence of the concentration factors for the low angle boundaries from the Flying Fox sample

is a sampling artefact; most of the LA-ICP-MS profiles have been focused on the deformation twin.

8. Discussion

Two types of element concentration are associated with microstructures. The first is related to the presence of cryptic fine-grained or buried pentlandite exsolution (Fig. 12), and is not considered further. The second, involving only the trace elements Pb, Bi and Ag, cannot be related to pentlandite micro-exsolution, is associated with crystal defects, and is independent on the amount of strain or metamorphic grade. Unlike Pb, Bi and Ag, elements such as As, and Co show uniform (or erratic) element profiles independently of the sample locality or geological history.

Two possible scenarios could explain correlation between trace elements and microstructures: 1) late hydrothermal fluid interaction with the sulphide phases and 2) intragrain diffusion. In first case, late hydrothermal fluid would have a role of introducing the elements (Pb, Bi and Ag) through fluid percolation and mineral-fluid reaction along the preferential diffusion pathways such as low angle, grain and deformation twin boundaries. This scenario was proposed for the serpentinisation process in peridotitic bodies from Leka Ophiolite Complex, Norway (Plümper et al., 2012). Plümper et al. (2012) showed that serpentinisation was initiated along olivine low angle boundaries and their data supported the hypothesis that water can ingress along dislocation walls as previously proposed by Boudier et al. (2010).

It is unlikely that the observed patterns of Pb, Bi and Au concentration in this study are related to precipitation along the intragrain microstructures from metamorphic fluid. Element concentrations at crystal defects are only observed in pyrrhotite, while percolating fluid would be expected to interact with all phases (e.g. compare Fig. 9a and Fig. 10e). Pervasive fracture systems transgressing grain boundaries are not observed at the scale of the observed

variations in element abundance. Parallel low angle boundaries in pyrrhotite from Perseverance are shown to be the result of plastic deformation (boundaries tilted along the low symmetry axes), rather than sealed fractures (Fig. 6). The average compositions of Pb, Bi and Ag, reported here are relatively similar in all three case studies (Fig. 8). Pentlandite occasionally appears along the low angle boundaries, however secondary low-temperature alteration phases such as mackinawite or violarite are absent. Finally, the localities that have been studied in this contribution are separated by several 100 km. It is unlikely that the same metamorphic fluid-related process would introduce additional Pb, Bi and Ag along described microstructures in all three ore bodies.

Intragrain diffusion is therefore the more likely interpretation. Information on intragrain diffusion coefficients of Pb, Bi and Ag in sulphides are scarce in the literature. However, these elements have larger atomic radii than other trace elements, such as Co and As, that do not show a correlation with observed microstructure (Shannon, 1976). It is likely, therefore, that their increased concentration along crystal defects is related to their low solubility, and this is a constraint on possible explanations.

Intragrain diffusion can take place by three different mechanisms: 1) volume diffusion, 2) high diffusivity pathway diffusion and 3) dislocation-impurity pair diffusion. These alternatives are investigated in turn.

Volume diffusion is a high temperature process (Klinger and Rabkin, 1999) whereby atoms migrate through a lattice in response to gradients in chemical potential. For volume diffusion to drive increased concentrations of Pb, Bi and Ag in microstructures by diffusion from the adjacent host grain, there would have to be a chemical potential gradient acting in the opposite direction to the concentration gradient. This is theoretically possible if there is a sufficiently strong effect of increase in point defects to cause a decrease in chemical potential large enough to offset the concentration contrast, but there is no evidence to support this.

The high diffusivity pathway diffusion model, on the other hand, involves already present dislocation arrays acting as "pipe" along which slow-diffusing components are able to preferentially migrate. Diffusion along high diffusivity pathways has been proposed in studies on reactions in garnet (Büttner and Kasemann, 2007), diffusion in zircons (Reddy et al., 2007; Timms et al., 2011); and for serpentinisation in olivines (Plümper et al., 2012) as previously noted. If this is the mechanism operating here, it requires that Pb, Bi and Ag are migrating into the host pyrrhotite along the high-diffusivity pathways, in response to some chemical potential gradient. It would require that these components are derived from an external phase, possibly an intergranular fluid component (Fig. 14a).

The interaction between dislocations and impurities is well known in material science and crystallography. It is generally accepted that the presence of impurities acts as a barrier to migration of the dislocations. However, Imai and Sumino (1983) suggest that the mobility of dislocations can increase with increasing concentration of impurities. Petukhov and Klyuchnik (2012) suggest that entrainment of impurities by moving dislocations results in the accumulation of impurities in dislocation cores. A dislocation-impurity pair (DIP) diffusion model requires that large ion impurities occupy dislocation cores and migrate with them during the recovery process, resulting in increased concentration of these impurities (e.g. Pb, Bi and Ag) along the newly formed dislocation arrays (Fig. 14b). Twin boundaries often contain pile-ups of dislocations (Kelly and Knowles, 2012), hence the model for the increased concentration of Pb, Bi and Ag along twin boundaries is consistent with the DIP model. This model requires no extraneous assumptions about chemical potential gradients and accounts for the restriction of increased concentrations to elements with high ionic radii; however, it is hindered by the limited understanding of dislocation-impurity kinetics. While the dislocation-impurity diffusion model cannot be discounted, the high diffusivity pathway

diffusion offers a simpler explanation for the observed features, and is the preferred hypothesis to explain them.

With Silver Swan reaching its metamorphic peak temperature at 300-350°C, it is evident that pyrrhotite still plastically deforms below these temperatures. The variation in the trace element concentration is dependent on the deformation mechanisms that are operating at the certain PT conditions as well as on the diffusion properties and the atomic radii of the trace elements. The study demonstrates that the mobility of large atomic radii trace elements, such as Pb, occurs even at low temperatures such as these.

8. Conclusion

This study of the komatiite hosted Ni sulphides sheds light on the diversity of the intragrain microstructures and their relationship with specific trace elements. Microstructural characterization of the massive Ni sulphides quantifies the diverse response of main sulphide phases to the deformation. Pyrite shows the least evidence of crystal plasticity, expressed as minor lattice distortion, while pentlandite grains express slightly higher degrees of lattice distortion and development of low angle boundaries. The weakest phase in magmatic sulphides is pyrrhotite, which records a range of diverse microstructures. Three different slip systems have been interpreted from EBSD data to be two basal slip systems: (0001)<11-20> and (0001)<10-10>; and a prism slip (11-20)<10-10>. Pyrrhotite can also contain deformation twins ((11-21)<10-10>) as observed in the Flying Fox sample.

The study illustrates the relationship between trace elements and microstructures in pyrrhotite. The variation in trace elements such As and Co is independent of microstructure. In contrast, Pb, Bi and Ag concentrations increase along grain boundaries, low angle boundaries and twin boundaries. This particular relationship between trace element chemistry and microstructure implies that these elements are subjected to intragrain diffusion during the

deformation and post-peak metamorphic conditions of the deposit, and that this particular style of trace element heterogeneity is restricted to the slowest diffusing, largest atomic radius elements. The likely mechanism is either dislocation-impurity pair diffusion or high diffusivity pathway diffusion. Element diffusion along the microstructures happens in all three cases, implying that for diffusion of these trace elements the main factor is the final disposition of the crystal defects. The presence and general similarity of increased trace element concentrations along low angle and twin boundaries in massive sulphides, in three samples of widely differing tectonic and metamorphic history, suggests that these processes occurred under low temperature, post-peak metamorphic conditions in each case. These results also reveal that large ions such as Pb, Bi and Ag can still diffuse at temperatures lower than 350°C.

Acknowledgments

The senior author was supported by the Commonwealth Scientific and Industrial Research Organisation (CSIRO) Office of the Chief Executive Scholarship, The University of Western Australia Scholarship for International Research Fees and a Top-up scholarship from Minerals and Energy Research Institute of Western Australia to Zoja Vukmanovic. We thank Dr Mark Pearce (CSIRO) and Dr Alistair White for helpful reviews of an early draft. This publication is an output from the CSIRO Minerals Down Under National Research Flagship, and is a contribution from the ARC Centre of Excellence for Core to Crust Fluid Systems. The authors acknowledge the facilities, scientific and technical assistance of the Australian Microscopy and Microanalysis Research Facility at the Centre for Microscopy, Characterisation and Analysis, The University of Western Australia, a facility funded by the University, State and Commonwealth Governments. This work was made possible in part by the OpenMIMS

software whose development is funded by the NIH/NIBIB National Resource for Imaging Mass Spectrometry, NIH/NIBIB 5P41 EB001974-10.

References

Ballhaus, C., Sylvester, P., 2000. Noble metal enrichment processes in the Merensky Reef, Bushveld Complex. Journal of Petrology 41, 545-561.

Barker, S.L.L., Hickey, K.A., Cline, J.S., Dipple, G.M., Kilburn, M.R., Vaughan, J.R., Longo, A.A., 2009. Uunlocking invisible gold: Use of NanoSims to evaluate gold, trace elements, and sulfur isotopes in pyrite from Carlin-type gold deposit. Economic Geology 104, 897-904.

Barnes, S.J., 2004. Introduction to nickel sulfide orebodies and komatiites of the Black Swan area, Yilgarn Craton, Western Australia. Mineralium Deposita 39, 679-683.

Barnes, S.J., 2006. Komatiite-hosted nickel sulfide deposits: geology, geochemistry, and genesis. Society of Economic Geologists Special Publication 13, 51-118.

Barnes, S.J., Anderson, J.A.C., Smith, T.R., Bagas, L., 2008. The Mordor Alkaline Igneous Complex, Central Australia: PGE-enriched disseminated sulfide layers in cumulates from a lamprophyric magma. Mineralium Deposita 43, 641-662.

Barnes, S.-J., Cox, R.A., Zientek, M.L., 2006. Platinum-Group Element, Gold, Silver and Base Metal Distribution in Compositionally Zoned Sulfide Droplets From the Medvezky Creek Mine, Noril'sk, Russia. Contributions to Mineralogy and Petrology 152, 187-200.

Barnes, S.J., Fiorentini, M.L., Duuring, P., Grguric, B.A., Perring, C.S., 2011. The Perseverance and Mount Keith Ni deposits of the Agnew-Wiluna Belt, Yilgarn Craton, Western Australia. Reviews in Economic Geology 17, 51-88.

Barnes, S.J., Gole, M.J., Hill, R.E.T., 1988. The Agnew nickel deposit, Western Australia: part I. Stratigraphy and structure. Econ. Geol. 83, 524-536.

Barnes, S.J., Wells, M.A., Verrall, M., 2009. Effects of Magmatic Processes, Serpentinization and Talc Carbonate Alteration on Sulfide Mineralogy and Ore Textures in The Black Swan Disseminated Nickel Sulfide Deposit, Yilgarn Craton., SGA Biennial Meeting, Townsville, Queensland.

Barrie, C.D., Boyle, A.P., Cox, S.F., Prior, D.J., 2009a. Slip systems and critical resolved shear stress in pyrite: an electron backscatter diffraction (EBSD) investigation. Mineral Mag 72, 1181-1199.

Barrie, C.D., Boyle, A.P., Salter, M., 2009b. How low can you go? - Extending downwards the limits of plastic deformation in pyrite. Mineralogic Magazine 73, 895-913.

Barrie, C.D., Pearce, M.A., Boyle, A.P., 2011. Reconstructing the pyrite deformation mechanism map. Ore Geology Reviews 39, 265-276.

Bekker, A., Barley, M.E., Fiorentini, M.L., Rouxel, O.J., Rumble, D., Beresford, S.W., 2009. Atmospheric sulfur in Archean komatiite-hosted nickel deposits. Science 326, 1086-1089.

Boudier, F., Baronnet, A., Mainprice, D., 2010. Serpentine Mineral Replacements of Natural Olivine and their Seismic Implications: Oceanic Lizardite versus Subduction-Related Antigorite. Journal of Petrology 51, 495-512.

Büttner, S.H., Kasemann, S.A., 2007. Deformation-controlled cation diffusion in tourmaline: A microanalytical study on trace elements and boron isotopes. American Mineralogist 92, 1862-1874.

Cassidy, K.F., Champion, D.C., Krapez, B.B., M.E., Brown, S.J.A., Blewett, R.S., Groenewald, P.B., Tyler, I.M., 2006. A revised geological framework for the Yilgarn Craton, Western Australia. Record 2006/8. Geological Survey of Western Australia, Perth, p. 8.

Clark, B.R., Kelly, W.C., 1973. Sulfide Deformation Studies; I, Experimental Deformation of Pyrrhotite and Sphalerite to 2,000 Bars and 500 degrees C. Economic Geology 68, 332-352.

Collins, J.E., Barnes, S.J., Hagemann, S.G., McCuaig, T.C., 2012a. Variability in Ore Composition and Mineralogy in the T4 and T5 ore shoots at the Flying Fox Ni-Cu-PGE Deposit, Yilgarn Craton, Western Australia Economic Geology 107, in press.
Collins, J.E., Hagemann, S.G., McCuaig, T.C., Frost, K.M., 2012b. Structural Controls on Sulfide Mobilization at the High-Grade Flying Fox Ni-Cu-PGE Sulfide Deposit, Forrestania Greenstone Belt, Western Australia. Economic Geology 107, 1433-1455.
Cowden, A., Archibald, N.J., 1987. Massive-sulfide fabrics at Kambalda and their relevance to the inferred stability of monosulfide solid-solution. The Canadian Mineralogist 25, 37-50.
Cox, S.F., 1987. Flow mechanisms in sulphide minerals. Ore Geology Reviews 2, 133-171.
Dare, S., Barnes, S.-J., Prichard, H., 2010. The distribution of platinum group elements (PGE) and other chalcophile elements among sulfides from the Creighton Ni–Cu–PGE sulfide deposit, Sudbury, Canada, and the origin of palladium in pentlandite. Mineralium Deposita, 1-29.
Dare, S.A.S., Barnes, S.-J., Prichard, H.M., Fisher, P.C., 2011. Chalcophile and platinum-group element (PGE) concentrations in the sulfide minerals from the McCreedy East deposit, Sudbury, Canada, and the origin of PGE in pyrite. Mineralium Deposita 46, 381-407.
Dowling, S.E., Barnes, S.J., Hill, R.E.T., Hicks, J.D., 2004. Komatiites and nickel sulfide ores of the Black Swan area, Yilgarn Craton, Western Australia. 2: Geology and genesis of the orebodies. Mineralium Deposita 39, 707-728.
Duuring, P., Bleeker, W., Beresford, S.W., Hayward, N., 2010. Towards a volcanic-structural balance: relative importance of volcanism, folding and remobilisation of nickel sulphides at the Perseverance Ni-Cu-(PGE) deposit. Mineralium Deposita 45, 281-311.
Farrell, S.P., Fleet, M.E., 2002. Phase separation in (Fe, Co)(sub1-x) S monosulfide solid-solution below 450 degrees C, with consequences for coexisting pyrrhotite and pentlandite in magmatic sulfide deposits. Canadian Mineralogist 40, 33-46.
Fiorentini, M., Beresford, S., Barley, M., Duuring, P., Bekker, A., Rosengren, N., Cas, R., Hronsky, J., 2012. District to camp controls on the genesis of komatiite-hosted nickel sulfide deposits, Agnew-Wiluna greenstone belt, Western Australia: Insights from the multiple sulfur isotopes. Economic Geology 107, 781-796.
Godel, B., Barnes, S.J., 2008. Image analysis and composition of platinum-group minerals in the J-M reef, Stillwater Complex. Economic Geology 103, 637-651.
Godel, B., Barnes, S.J., Maier, W.D., 2007. Platinum-group elements in sulphide minerals, platinum-group minerals, and whole-rocks of the Merensky Reef (Bushveld Complex, South Africa): Implications for the formation of the reef. Journal of Petrology 48, 1569-1604.
Godel, B., González-Álvarez, I., Barnes, S.J., Barnes, S.-J., Parker, P., Day, J., 2012. Sulfides and Sulfarsenides from the Rosie Nickel Prospect, Duketon Greenstone Belt, Western Australia. Economic Geology 107, 275-294.
Gole, M.J., Barnes, S.J., Hill, R.E.T., 1987. The role of fluids in the metamorphism of komatiites, Agnew nickel deposit, Western Australia. Contributions to Mineralogy and Petrology 96, 151-162.
Goscombe, B., Blewett, R.S., Czarnota, K., Groenewald, P.B., Maas, R., 2009. Metamorphic evolution and integrated terrane analysis of the eastern Yilgarn Craton; rationale, methods, outcomes and interpretation. Geoscience Australia Record 2009/23, 1-270.
Groves, D.I., Barrett, F.M., McQueen, K.G., 1979. The relative roles of magmatic segregation, volcanic exhalation and regional metamorphism in the generation of volcanic-associated nickel ores of Western Australia. Canadian Mineralogist 17, 319-336.
Hanley, J.J., 2007. The role of arsenic-rich melts and mineral phases in the development of high-grade Pt-Pd mineralization within komatiite-associated magmatic Ni-Cu sulfide horizons at Dundonald Beach South, Abitibi Subprovince, Ontario, Canada. Economic geology and the Bulletin Of the Society Of Economic Geologists 102, 305-317.

Hellstrom, J., Paton, C., Woodhead, J., Hergt, J., 2008. Iolite: software for spatially resolved LA (quad and MC) ICPMS analysis. Mineralogical association of Canada short course series 40, 343-348.
Hill, R.E.T., 1984. Experimental study of phase relations at 600oC in a portion of the Fe-Ni-Cu-S system and its application to natural sulphide assemblages, in: Buchanan, D.L., Jones, M.J. (Eds.), Sulphide deposits in mafic and ultramafic rocks. Institute of Mining and Metallurgy, London, pp. 14-21.
Hill, R.E.T., Barnes, S.J., Dowling, S.E., Thordarson, T., 2004. Komatiites and nickel sulphide orebodies of the Black Swan area, Yilgarn Craton, Western Australia. 1. Petrology and volcanology of host rocks. Mineralium Deposita 39, 684-706.
Holwell, D.A., McDonald, I., 2007. Distribution of platinum-group elements in the Platreef at Overysel, northern Bushveld Complex: a combined PGM and LA-ICP-MS study. Contributions to Mineralogy and Petrology 154, 171-190.
Huminicki, M.A.E., Sylvester, P.J., Carbi, L.J., Lesher, C.M., Tubrett, M., 2005. Quantitative Hass Balance of Platinum Group Elements in the Kelly Lake Ni-Cu-Pge Deposit Copper Cliff Offset, Sudbury. Economic Geology 100, 1631-1646.
Huppert, H.E., Sparks, R.S.J., 1985. Komatiites I: Eruption and Flow. Journal of Petrology 26, 694-725.
Huppert, H.E., Sparks, R.S.J., Turner, J.S., Arndt, N.T., 1984. Emplacement and cooling of komatiite lavas. Nature 309, 19-22.
Imai, M., Sumino, K., 1983. In situ X-ray topographic study of the dislocation mobility in high-purity and impurity-doped silicon crystals. Philosophical Magazine A 47, 599-621.
Keller, L.M., Abart, R., Wirth, R., Schmid, D.W., Kunze, K., 2006. Enhanced mass transfer through short-circuit diffusion: Growth of garnet reaction rims at eclogite facies conditions. American Mineralogist 91, 1024-1038.
Kelly, A., Knowles, K.M., 2012. Twinning, Crystallography and Crystal Defects. John Wiley & Sons, Ltd, pp. 335-361.
Kelly, W.C., Clark, B.R., 1975. Sulfide deformation studies; III, Experimental deformation of chalcopyrite to 2,000 bars and 500 degrees C. Economic Geology 70, 431-453.
Klinger, L., Rabkin, E., 1999. Beyond the Fisher model of grain boundary diffusion: effect of structural inhomogeneity in the bulk. Acta Materialia 47, 725 - 734.
Kullerud, G., Yund, R.A., Moh, G.H., 1969. Phase relations in the Cu-Fe-S,Cu-Ni-S and Fe-Ni-S systems, in: Wilson, H.D.B. (Ed.), Magmatic Ore Deposits, Economic Geology Monograph 4, pp. 323-343.
Lesher, C.M., Arndt, N.T., Groves, D.I., 1984. Genesis of komatiite-associated nickel sulphide deposits at Kambalda Western Australia: a distal volcanic model, in: Buchanan, D.L., Jones, M.J. (Eds.), Sulphide deposits in mafic and ultramafic rocks. Institute of Mining and Metallurgy, London, pp. 70-80.
Lloyd, G.E., 2004. Microstructural evolution in a mylonitic quartz simple shear zone: the significant roles of dauphine twinning and misorientation. Special publication - Geological Society of London 224, 39-61.
Lloyd, G.E., Freeman, B., 1994. Dynamic recrystallization of quartz under greenschist conditions. Journal of Structural Geology 16, 867-881.
Mark, D.F., Kelley, S.P., Lee, M.R., Parnell, J., Sherlock, S.C., Brown, D.J., 2008. Ar–Ar dating of authigenic K-feldspar: Quantitative modelling of radiogenic argon-loss through subgrain boundary networks. GEOCHIMICA ET COSMOCHIMICA ACTA 72, 2695-2710.
Marston, R.J., 1984. Nickel mineralization in Western Australia. Geological Survey of Western Australia Mineral Resources Bulletin 14, 271.
McQueen, K.G., 1979a. Experimental heating and diffusion effects in Fe-Ni sulphide ore from Redross, Western Australia. Economic Geology 74, 140-148.

McQueen, K.G., 1979b. Metamorphism and deformation of volcanic associated nickel deposits: a study of mineralization around the Widgiemooltha Dome, Western Australia. University of Western Australia, Nedlands, p. 280.
McQueen, K.G., 1987. Deformation and remobilization in some Western Australian nickel ores. Ore Geology Reviews 2, 269-286.
Naldrett, A., Craig, J., Kullerud, G., 1967. The central portion of the Fe-Ni-S system and its bearing on pentlandite exsolution in iron-nickel sulfide ores. Economic Geology 62, 826-847.
Naldrett, A.J., 2004. Magmatic Sulfide Deposits: Geology, Geochemistry and Exploration. Springer, Heidelberg.
Naldrett, A.J., Kullerud, G., 1967. The Fe-Ni-S system - limits of the Fe(1-x)-Ni(1-x)S solid solution between 600 and 250oC. Carnegie Institute of Washington Yearbook 65, 320-326.
Passchier, C.W., Trouw, R.A.J., 2005. Microtectonics. Springer, Germany.
Perring, C.S., Barnes, S.J., Hill, R.E.T., 1995. The physical volcanology of Archaean komatiite sequences from Forrestania, Southern Cross Province, Western Australia. Lithos 34, 189-207.
Perring, C.S., Barnes, S.J., Hill, R.E.T., 1996. Geochemistry of Archaean komatiites from the Forrestania Greenstone Belt, Western Australia: evidence for supracrustal contamination. Lithos 37, 181-197.
Petukhov, B.V., Klyuchnik, P.A., 2012. Dynamic interaction of dislocations with impurity subsystem in crystalline materials. Crystallography Reports 57, 388-392.
Piña, R., Gervilla, F., Barnes, S.-J., Ortega, L., Lunar, R., 2013. Platinum-group elements-bearing pyrite from the Aguablanca Ni-Cu sulphide deposit (SW Spain): a LA-ICP-MS study. Eur J Mineral.
Piña, R., Gervilla, F., Barnes, S.J., Ortega, L., Lunar, R., 2012. Distribution of platinum-group and chalcophile elements in the Aguablanca Ni–Cu sulfide deposit (SW Spain): Evidence from a LA-ICP-MS study. Chemical Geology 302–303, 61-75.
Plümper, O., King, H., Vollmer, C., Ramasse, Q., Jung, H., Austrheim, H., 2012. The legacy of crystal-plastic deformation in olivine: high-diffusivity pathways during serpentinization. Contributions to Mineralogy and Petrology 163, 701-724.
Porter, D.J., McKay, K.G., 1981. The nickel sulphide mineralization and metamorphic setting of the Forrestania area, Western Australia. Economic Geology 76, 1524-1549.
Prior, D.J., Boyle, A.P., Brenker, F., Cheadle, M.C., Day, A., Lopez, G., Peruzzo, L., Potts, G.J., Reddy, S., Spiess, R., Timms, N.E., Trimby, P., Wheeler, J., Zetterstrom, L., 1999. The application of electron backscatter diffraction and orientation contrast imaging in the SEM to textural problems in rocks. American Mineralogist 84, 1741-1759.
Reddy, S., Potts, G., Kelley, S., 2001. 40Ar/39Ar ages in deformed potassum feldspar: evidence of microstructural control on Ar isotope systematics. Contributions to Mineralogy and Petrology 141, 186 - 200.
Reddy, S.M., Timms, N.E., Pantleon, W., Trimby, P., 2007. Quantitative characterization of plastic deformation of zircon and geological implications. Contributions to Mineralogy and Petrology 153, 625-645.
Reddy, S.M., Timms, N.E., Trimby, P., Kinny, P.D., Buchan, C., Blake, K., 2006. Crystal-plastic deformation of zircon: A defect in the assumption of chemical robustness. Geology 34, 257-260.
Seat, Z., Stone, W.E., Mapleson, D.B., Daddow, B.C., 2004. Tenor variation within komatiite-associated nickel sulphide deposits: insights from the Wannaway Deposit, Widgiemooltha Dome, Western Australia. Mineralogy and Petrology 82, 317-339.
Shannon, R., 1976. Revised effective ionic radii and systematic studies of interatomic distances in halides and chalcogenides. Acta Crystallographica Section A 32, 751-767.

Sugaki, A., Kitakaze, A., 1998. High form of pentlandite and its thermal stability. American Mineralogist 83, 133-140.
Timms, N., Kinny, P., Reddy, S., 2006. Enhanced diffusion of Uranium and Thorium linked to crystal plasticity in zircon. Geochemical Transactions 7, 10.
Timms, N.E., Kinny, P.D., Reddy, S.M., Evans, K., Clark, C., Healy, D., 2011. Relationship among titanium, rare earth elements, U–Pb ages and deformation microstructures in zircon: Implications for Ti-in-zircon thermometry. Chemical Geology 280, 33-46.
Timms, N.E., Li, J., Reddy, S.M., 2009. Quantitative microstructural characterization of natrojarosite scale formed during high-pressure acid leaching of lateritic nickel ore. American Mineralogist 94, 1111-1119.
Timms, N.E., Reddy, S.M., Fitz Gerald, J.D., Green, L., Muhling, J.R., 2012. Inclusion-localised crystal-plasticity, dynamic porosity, and fast-diffusion pathway generation in zircon. Journal of Structural Geology 35, 78-89.
Trimby, P.W., Prior, D.J., Wheeler, J., 1998. Grain boundary hierarchy development in a quartz mylonite. Journal of Structural Geology 20, 917-935.

Figure captions

Figure 1 Simplified geological map of part of the Yilgarn craton, Western Australia, showing locations of the three komatiite hosted Ni deposits studied in this contribution Geological data is from the Geological Survey of Western Australia on-line database (http://www.doir.wa.gov.au/aboutus/geoview_launch.asp).

Figure 2 geological maps and sections of the study sites. a) Geological map of Black Swan ultramafic complex, modified from Barnes et al. 2004. b) 900m level plan showing morphology and distribution of the Silver Swan (SS) ore shoot modified from Dowling et al. 2004. c) Geology and location of the Perseverance deposit, Duuring et al. 2010. d) Perseverance level plan, 3220 m below surface modified after Barnes et al. 2011. e) Simplified geological map of a section of the Forrestania greenstone belt, showing the location of Flying Fox Ni deposits. Map is modified after Collins et al. 2012. f) Cross section of the T0 and T1 ore body from Flying Fox modified from Collins et al. 2012. Black triangle represents approximate location of the samples.

Figure 3. a) Schematic representation of a tilt boundary. b) Schematic representation of a twist boundary. c) Schematic stereographic plot where pole to slip plane, slip direction and rotation axis are orthogonal to each other. Pole to slip plane and rotation axis are contained along the trace of the boundary wall. d) Schematic stereographic plot of the rotation axis and its relationship to the slip plane.

Figure 4 a-b) Photomicrograph of the sample from the Silver Swan ore body; c-d) Photomicrograph of the Perseverance sample; e-f) Photomicrograph of the sample from Flying Fox deposit. White arrows indicate deformation twins in pyrrhotite grain. Po –

pyrrhotite, pn – pentlandite, py – pyrite, amp – amphibole, cal – calcite, mt – magnetite, qtz – quartz.

Figure 5 Electron backscatter diffraction data from the Silver Swan sample. Areas SS1 and SS2 correspond to the position of laser ablation ICP-MS profiles presented later in the text. a) Band contrast – grain boundary map of the pyrrhotite grain. Grain boundaries are classified by their angle and are coloured accordingly. b) Band contrast – misorientation axis orientation map of the pyrrhotite grain. c) Band contrast – cumulative misorientation map for the pyrrhotite grain. Maximum misorientation from the reference point (red cross) is 35°. Enhanced area of two boundaries (1 and 2) later referred to in (f) and (g). d) Band contrast – cumulative misorientation map for the pyrite grain. Maximum lattice misorientation is 4°). e) Stereographic projection of pole figures (1) and stereographic projection of rotation axes (2) of the pyrrhotite grain. Data is plotted on the lower hemisphere equal area projection. f) Pole figure data of the boundary 1 from the (c 1) (left) and its rotation axis (right). g) Pole figure data of the boundary 2a and 2b from the (c 2) (left) and its rotation axes (right). Trace boundary of the boundary 2b can be plotted in two ways that both contain the rotation axis.

Figure 6 Electron backscatter diffraction data from the Perseverance sample. “Percy 1” and “Percy 2” represent position of the laser ablation lines later referred to in the text a) Inverse pole figure-band contrast map for the pyrrhotite grain relative to the X (horizontal) direction of the sample reference plane. White lines indicate position of the grains shown on (b). b) Cumulative misorientation –grain boundary-band contrast map for the pyrrhotite grains (1-4) and a pentlandite grain (5). Maximum of cumulative misorientation for the pyrrhotite grains from the arbitrary reference point (red cross) is 15° and 5° for the pentlandite grain. Red open areas indicate the position of the examined low angle boundaries from e, f and g. c) Stereographic projection of the pole figure data plotted on the lower hemisphere –equal area projection for pyrrhotite (1-4) and pentlandite (5). d) Stereographic projection of the rotation

axes for respective grain (1-5). e) Enhanced area of low angle boundary 1 (right) from grain 2 (b), pole figure data of the low angle boundary 1 (central) and rotation axes of the low angle boundary 1 (left).). f) Enhanced area of low angle boundary 2 (right) from grain 2 (b), pole figure data of the low angle boundary 2 (central) and rotation axes of the low angle boundary 2 (left).). g) Enhanced area of pentlandite low angle boundary 3 (right) from grain 5 (b), pole figure data of the low angle boundary 3 (central) and rotation axes of the low angle boundary 3 (left).

Figure 7 a) Inverse pole figure- grain boundary-and contrast map for the Flying Fox sample. Inverse pole figure shows orientation of the pyrrhotite grains respective to the X (horizontal) direction of the sample reference frame. White line highlights location of the pentlandite (e). Cumulative misorientation map of the pyrrhotite host (b) and twin (c) with maximum lattice misorientation of 15° from the arbitrary reference point (red cross). d) Lower hemisphere-equal area projection of the pyrrhotite pole figure data (1). Data is colour coded according to the map (b). Stereographic projection of the 2-15° rotation axes (2) and 15-90° rotation axes (3) in host and twin pyrrhotite grains. e) cumulative misorientation – grain boundary – band contrast map for the pentlandite (1) with maximum misorientation of 5° from the reference point. Pentlandite pole figure data (2) and contour plot of 2-10° rotation axes (3). f) Misorientation angle distribution histogram for the pyrrhotite grains. Two peaks on the histogram correspond to four different crystal rotation axes classified by the degree of misorientation. Crystallographic orientation of the ~85° axis corresponds to the crystal axis (10-10). g) Misorientation angle distribution histogram for the pentlandite grains. h) Schematic representation of the pyrrhotite twins with their rotation axis (red line, <10-10>). i) Schematic reconstruction of the pyrrhotite twin's crystallographic parameters (left) and pole figure data for the axes <11-21> (right).

Figure 8 Box-Whisker diagrams showing distribution of trace element concentrations in pyrrhotite (yellow), pentlandite (red) and pyrite (blue) for the massive sulphides from Silver Swan, Perseverance and Flying Fox deposits. Number of analysis for 1) Silver Swan: po (94), pn (25) and py (6); 2) Perseverance: po (105), pn (47) and c) Flying Fox: po (88), pn (30) and py (45). Box-Whiskers plots show minimum, maximum, median, lower quartile, and upper quartile information for groups of data.

Figure 9 Laser ablation ICP-MS profiles along lines 1 and 8 in Silver Swan pyrrhotite (Figure 3a). Elements Co, As, Ag, Pb and Bi are plotted against the length of the profile for line SS1 (A-D) and for line SS2 (E-H). Gray area on each plot corresponds to the maximum local misorientation along the respective profile. Detection limits for Co, As, Ag, Pb and Bi are presented in the electronic appendix. Detection limits for corresponding elements are shown in table 1. Values below detection limits are plotted at zero ppm

Figure 10 Laser ablation ICP-MS profiles along lines Percy 1 and Percy 2 along pyrrhotite (A-D) and pentlandite (F-E) from the sample coming from Perseverance deposit (Figure 4a). Elements Co, As, Ag, Pb and Bi are plotted against the length of respective profiles. Gray area on each plot is defined by the local misorientation peak along the respective profile. Detection limits for Co, As, Ag, Pb and Bi are presented in electronic appendix. Detection limits for corresponding elements are shown in table 1.

Figure 11 Laser ablation ICP-MS profiles along lines FF1 and FF2 along pyrrhotite grain from Flying Fox (Figure 5a). Elements Co, As, Ag, Pb and Bi are plotted against the length of respective profiles. Gray area on each plot is defined by the peak in local misorientation along the respective profile. Detection limits for Co, As, Ag, Pb and Bi are presented in electronic appendix. Detection limits for corresponding elements are shown in table 1.

Figure 12 Laser ablation ICP-MS and NanoSims element maps for the Flying Fox sample (A). Black dotted line highlights position of the twin boundaries in pyrrhotite grain. b-g) Laser ablation ICP –MS Cobalt, Cu, Ag, Pb and Bi element maps, all expressed in relative ppm abundance. f-i) NanoSims element maps for Pb and Ag.

Figure 13 Box-whisker diagrams showing peak/background ratio for each element along various category of boundary: high grain boundaries (HGB), boundaries with more than 15° of rotation along mixed rotation axes (<15 mix), boundaries with more than 15° of rotation along <11-20> rotation axis (<15 m), boundaries with more than 15° of rotation along <10-10> rotation axis (<15 a), boundaries with more than 10° of rotation along mixed rotation axes (<10 mix), boundaries with more than 10° of rotation along <11-20> rotation axis (<10 m), boundaries with more than 10° of rotation along <10-10> rotation axis (<10 a) and twin boundaries (TW). Ratio was calculated using equation (½ln(peak/background)) by Pawlowsky-Glahn and Egozcue (2006). Negative values of "peak to background" ratio indicate that no peak is observed at the specific boundary.

Figure 14 Schematic representations of two diffusion models: a) high diffusivity pathway model "*pipe diffusion*" where trace element diffuse form intergranular fluid or Pb/Ag/Bi rich phase along the grain, low angle and twin boundaries; and b) dislocation-impurity pair "*DIP*" diffusion where dislocations carry large ions (Pb, Bi and Ag) during the recovery process when they form low angle boundary or pile-up along grain and twin boundaries.

Table 1 Estimation of LA–ICP-MS detection limits. Po-pyrrhotite; pn –pentlandite; py – pyrite.

Figure 1

Click here to download high resolution image

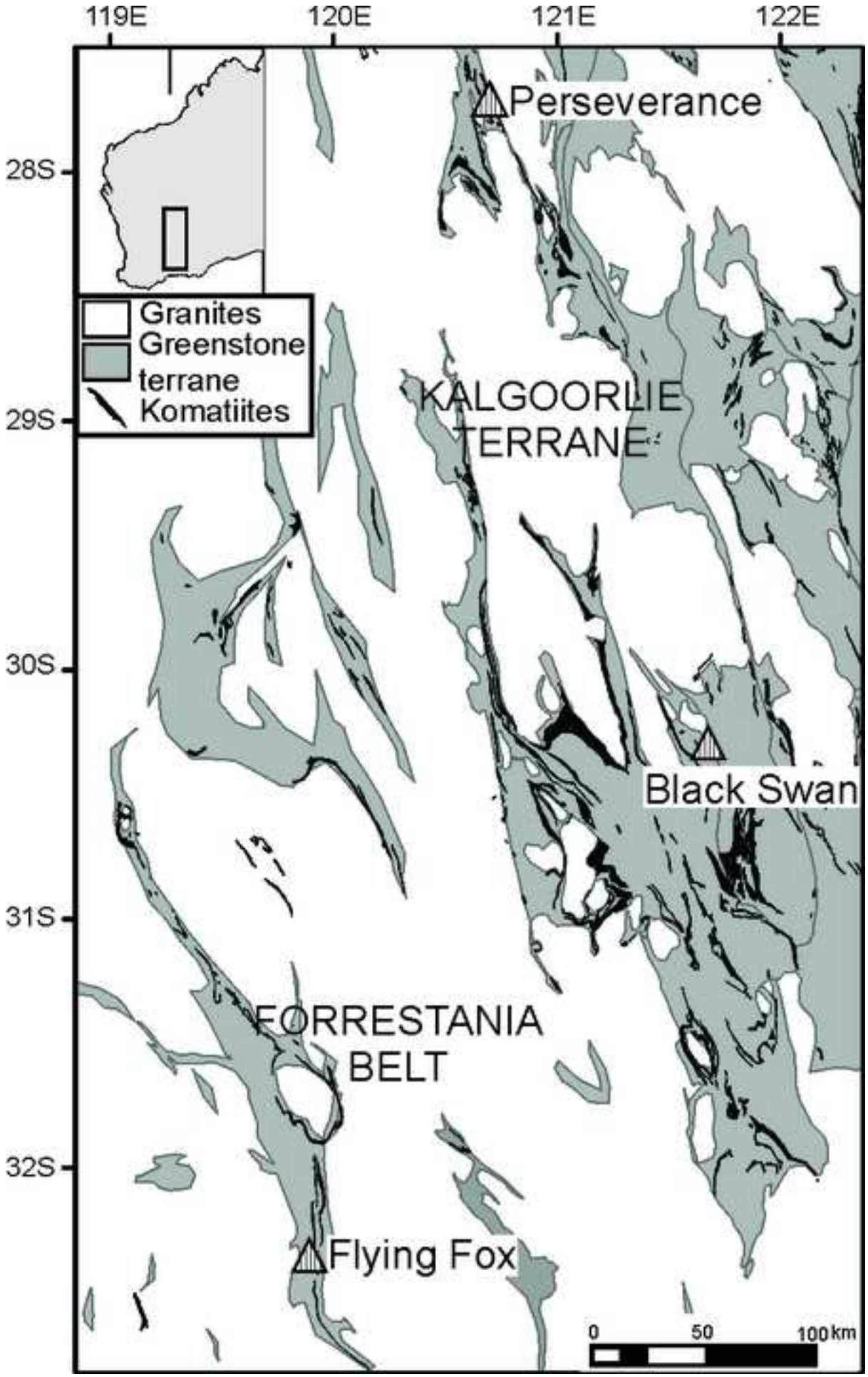

Figure 2

Click here to download high resolution image

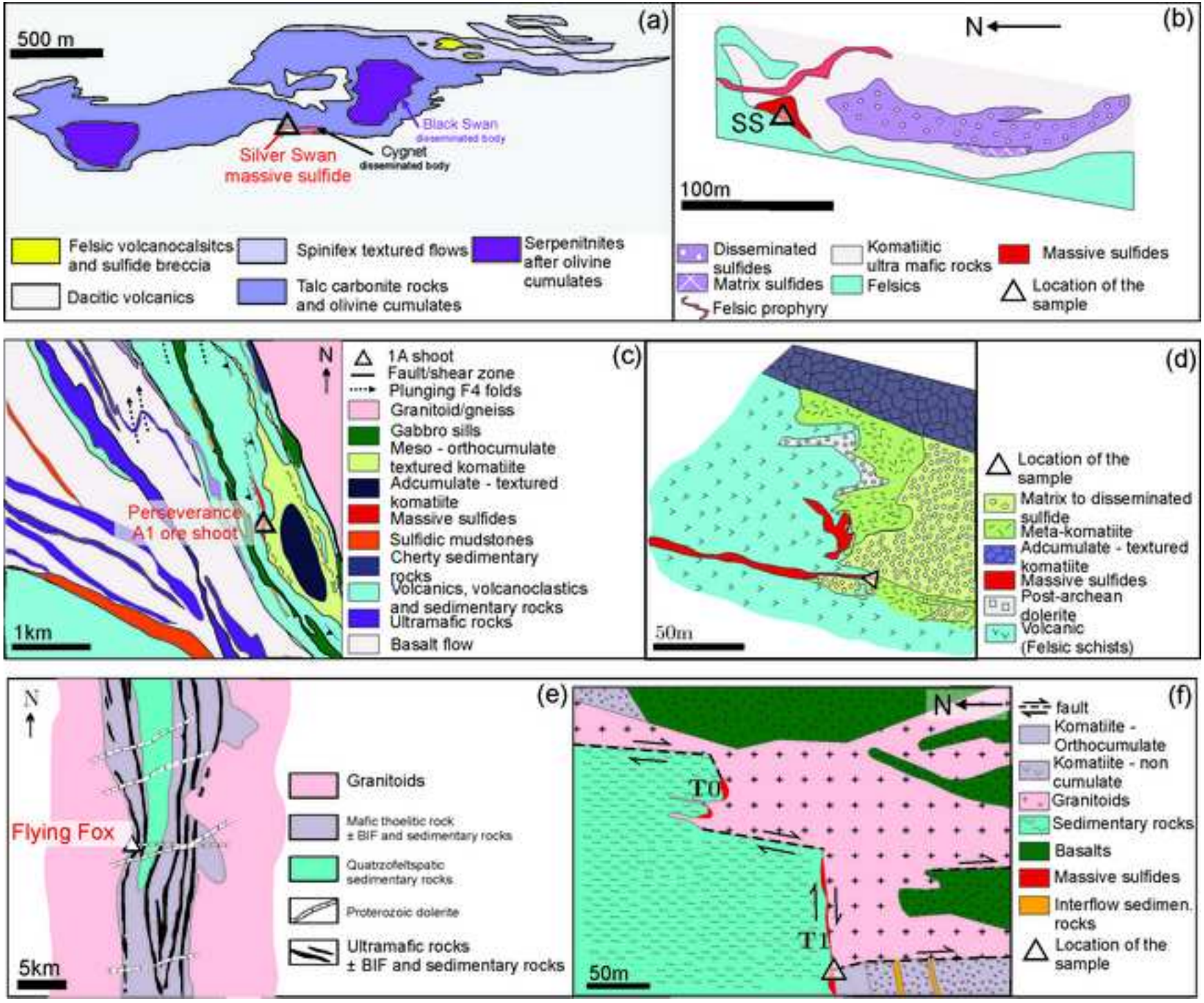

Figure 3

Click here to download high resolution image

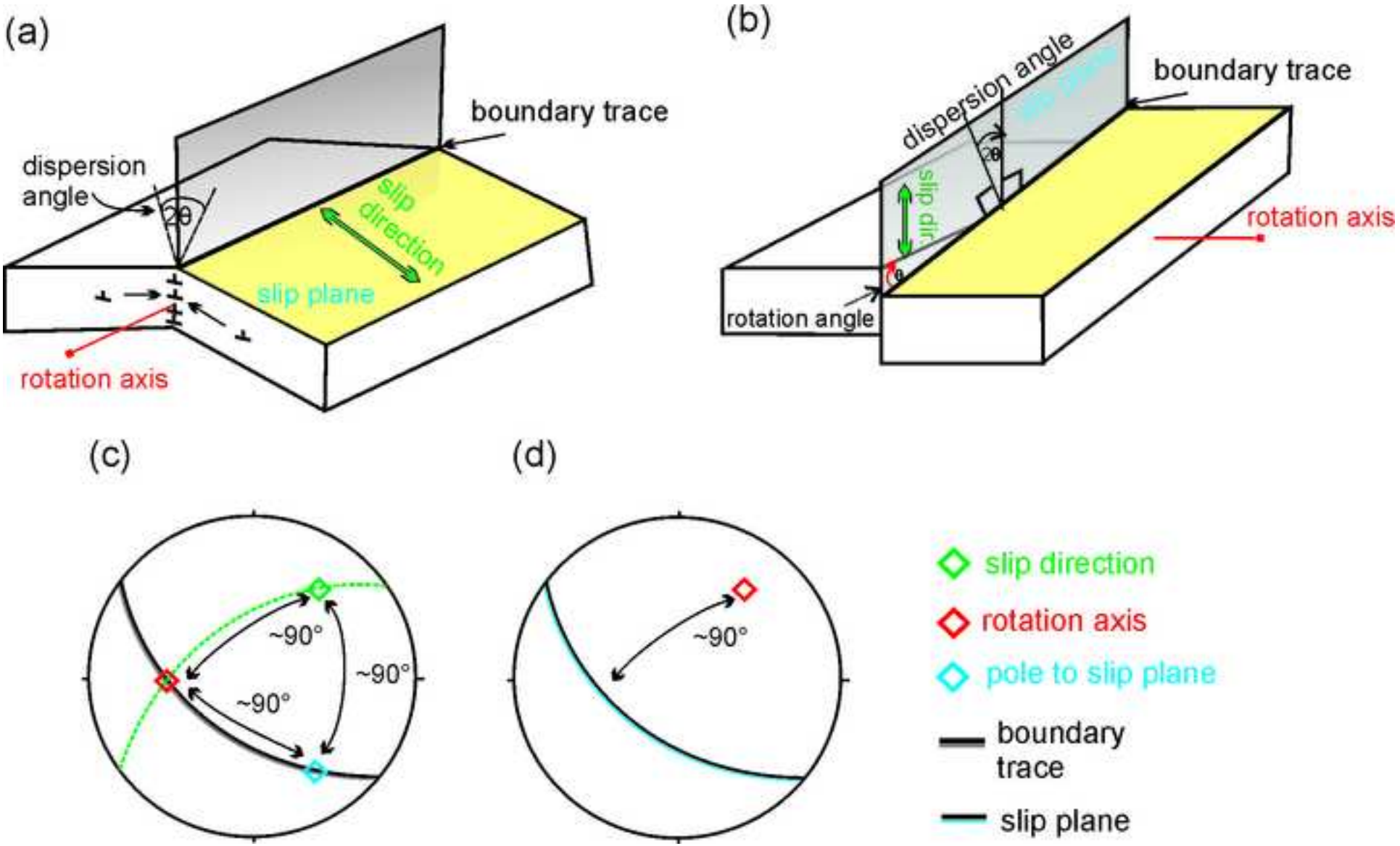

Figure 4

Click here to download high resolution image

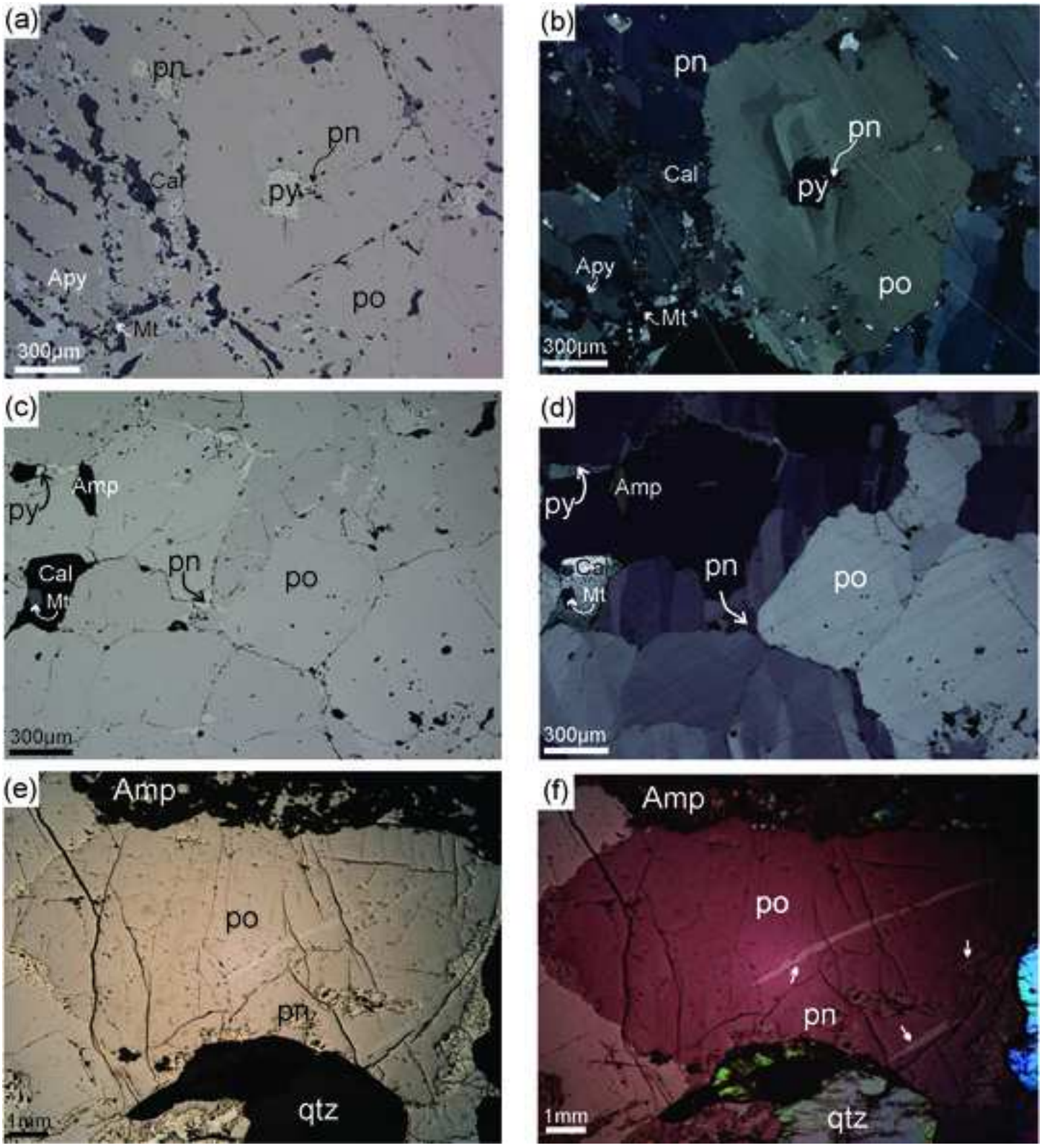

Figure 5

Click here to download high resolution image

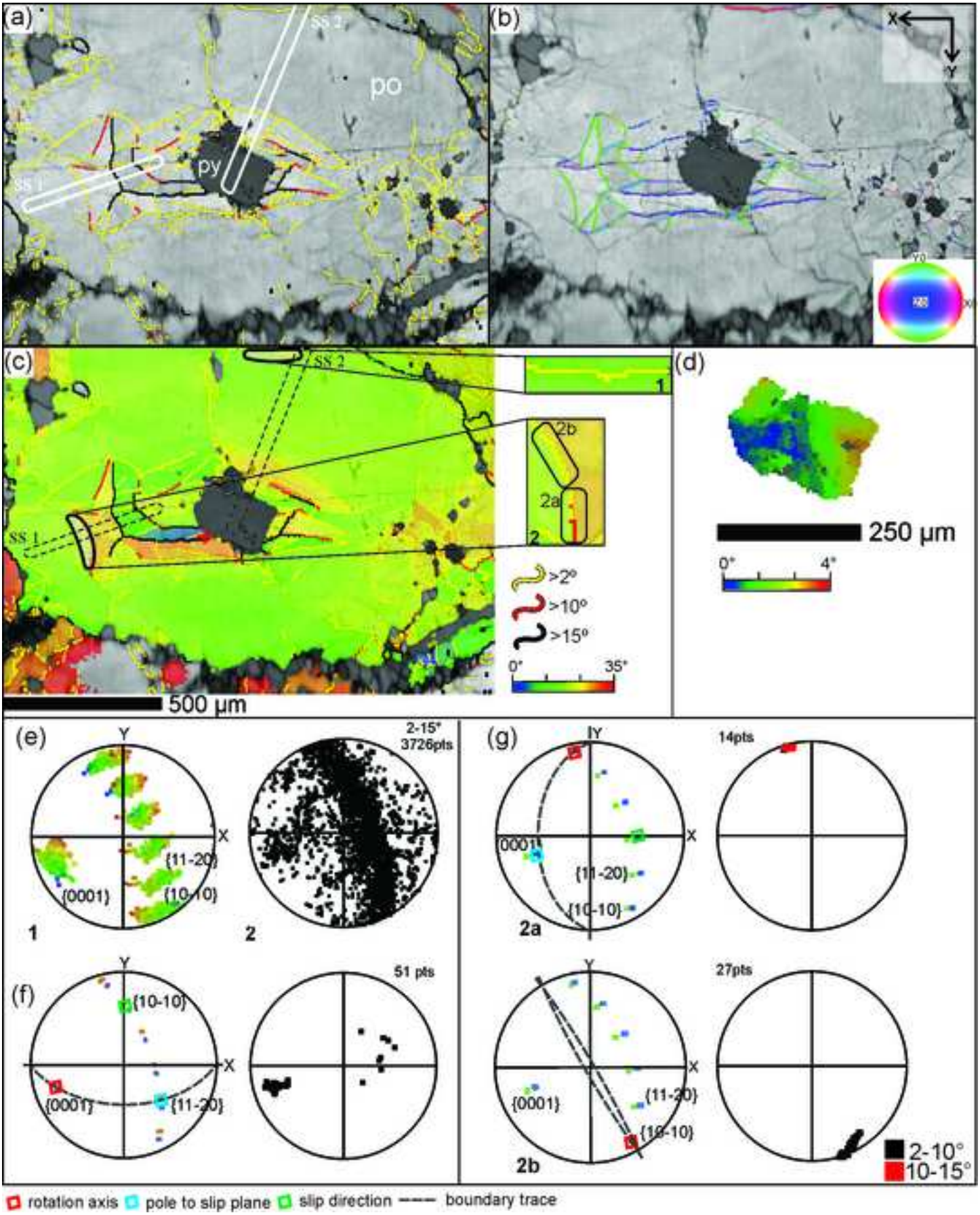

Figure 6

Click here to download high resolution image

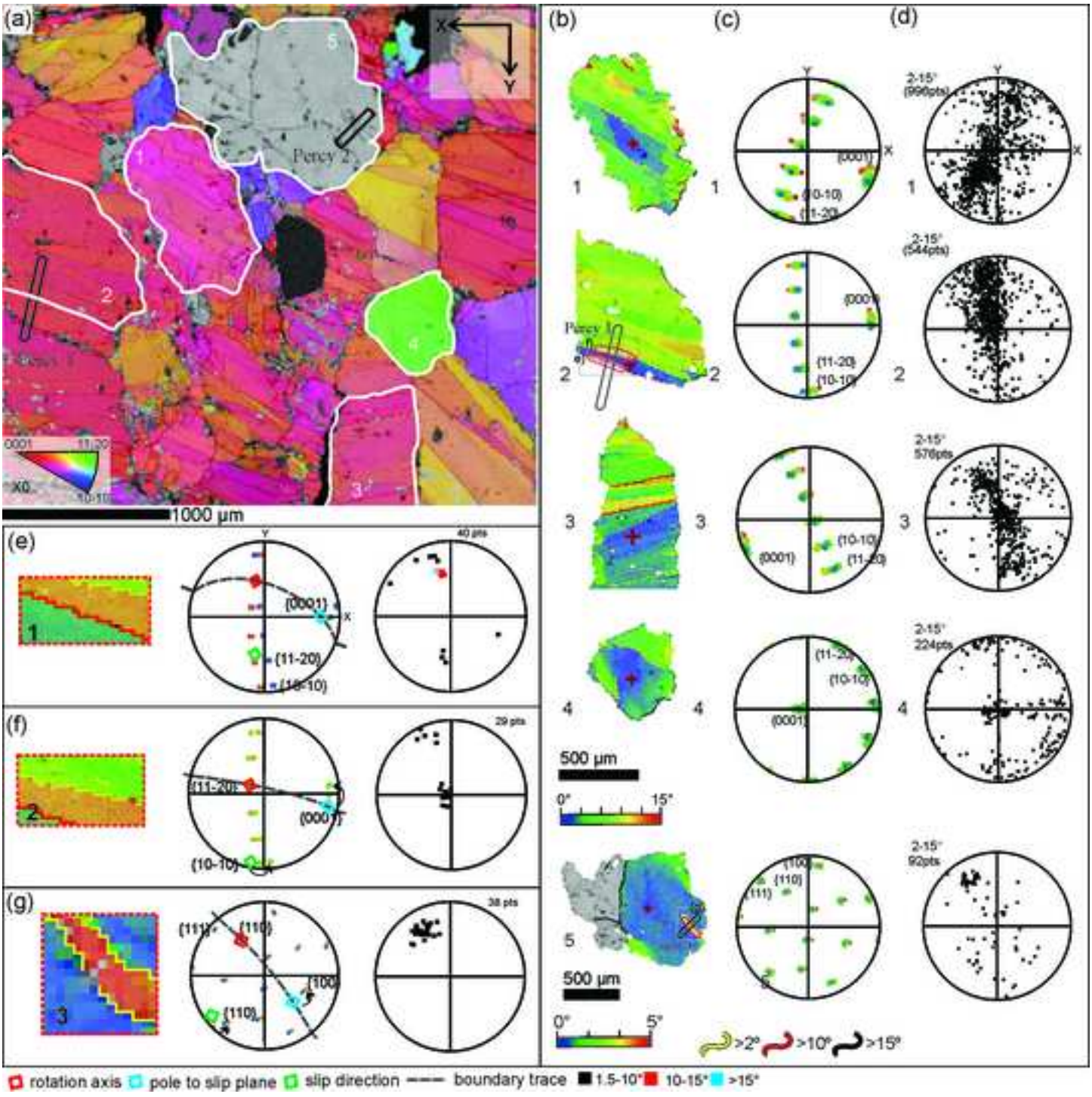

Figure 7

Click here to download high resolution image

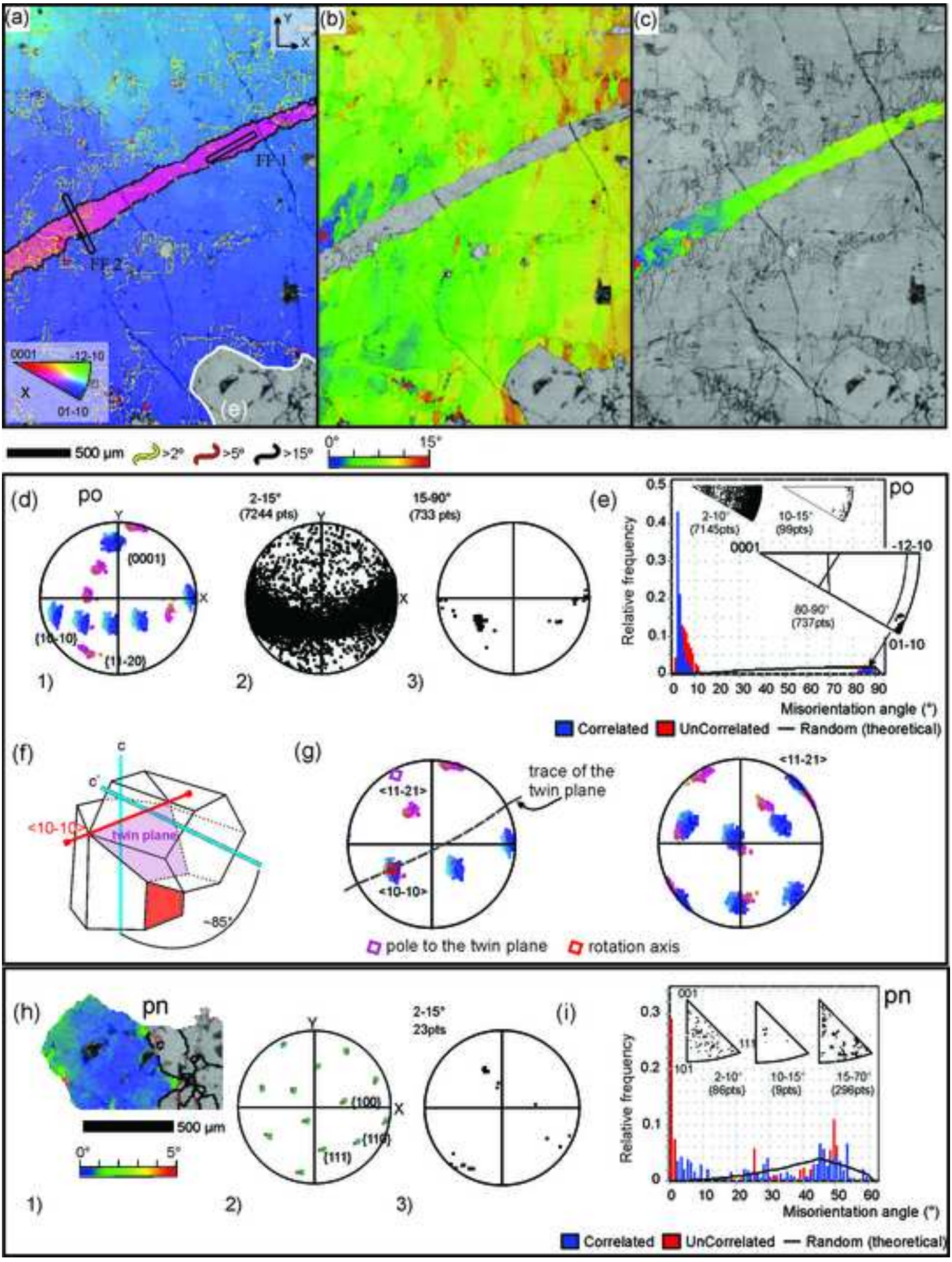

Figure 8

Click here to download high resolution image

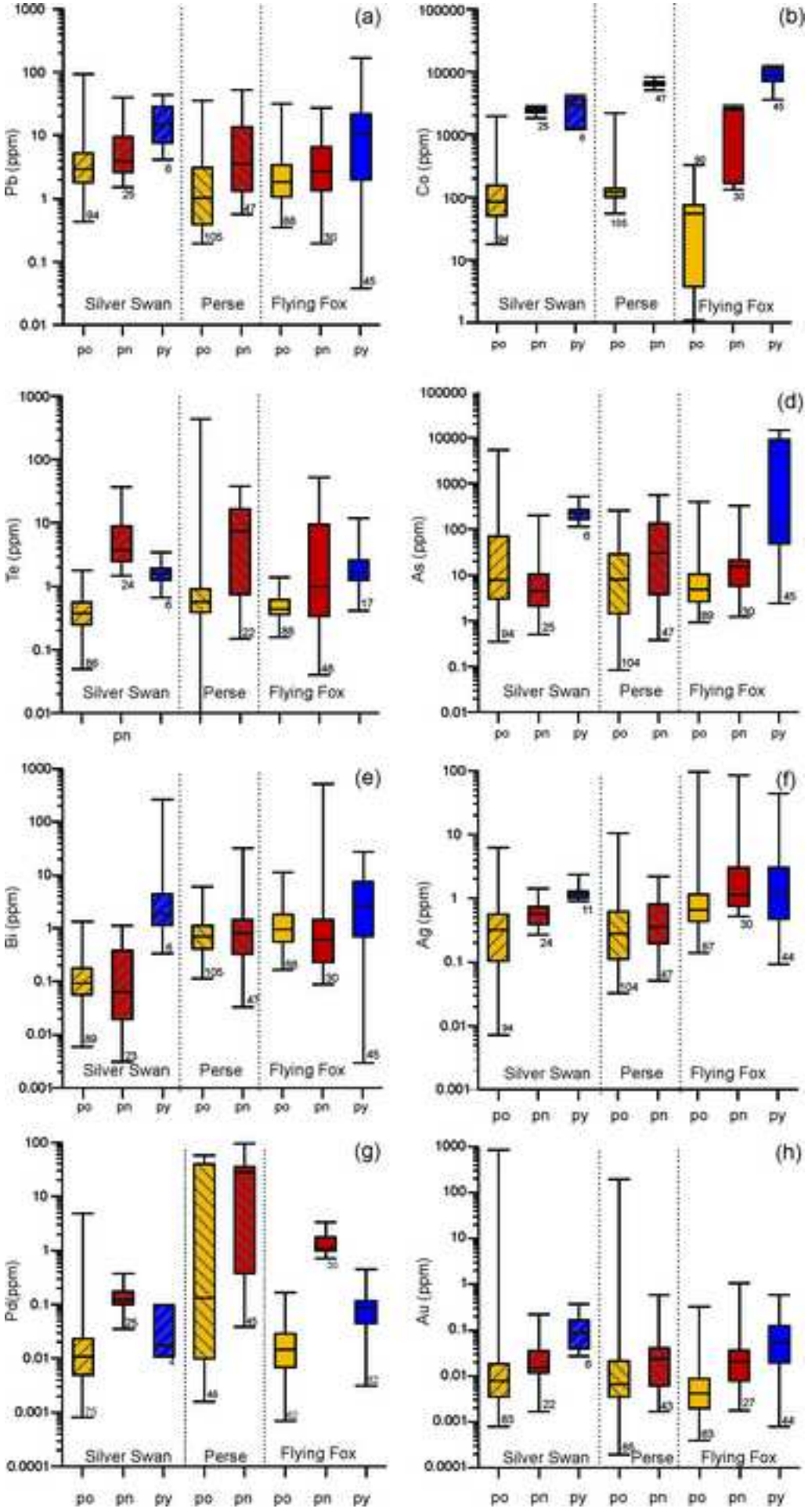

Figure 9

Click here to download high resolution image

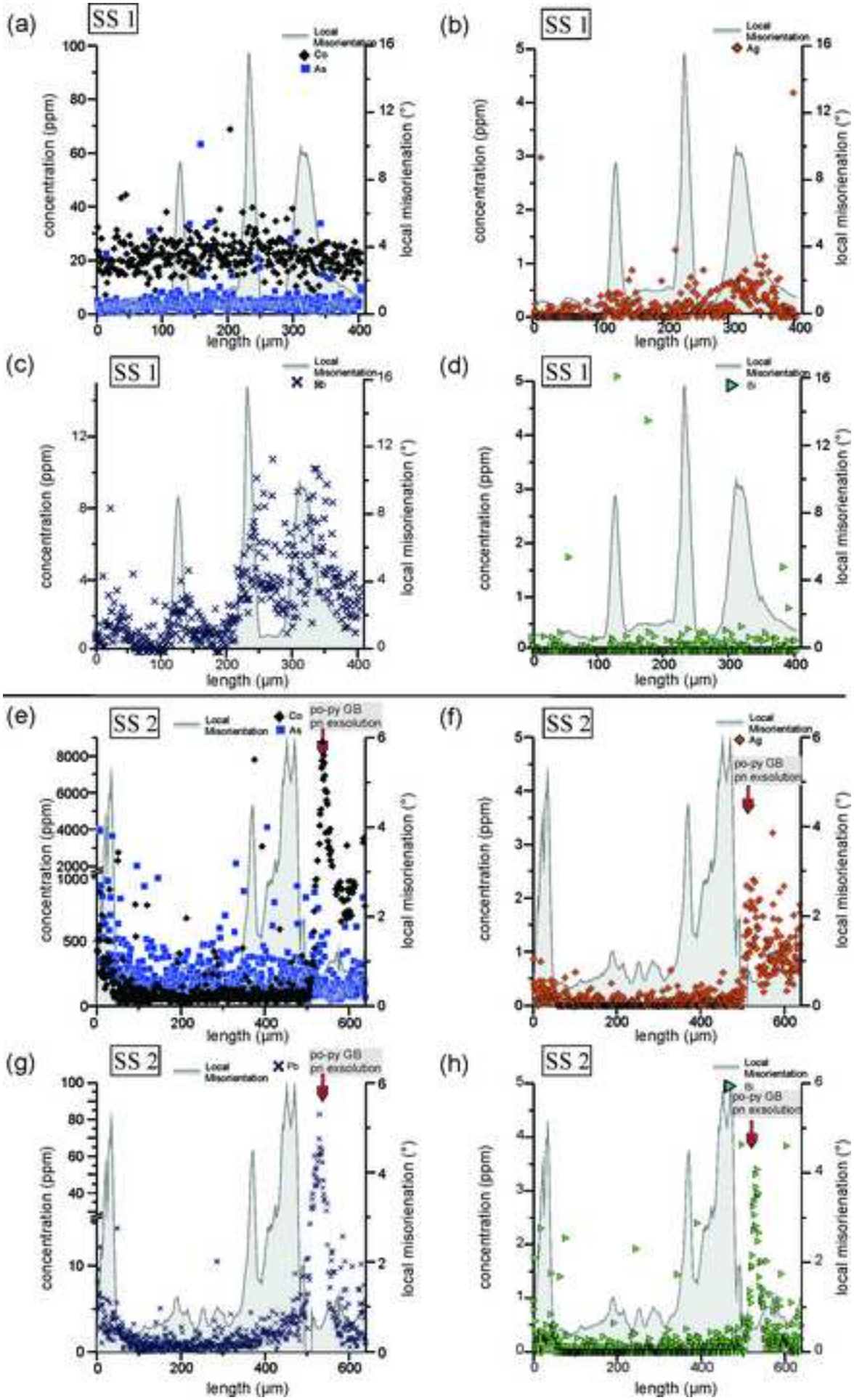

Figure 10

Click here to download high resolution image

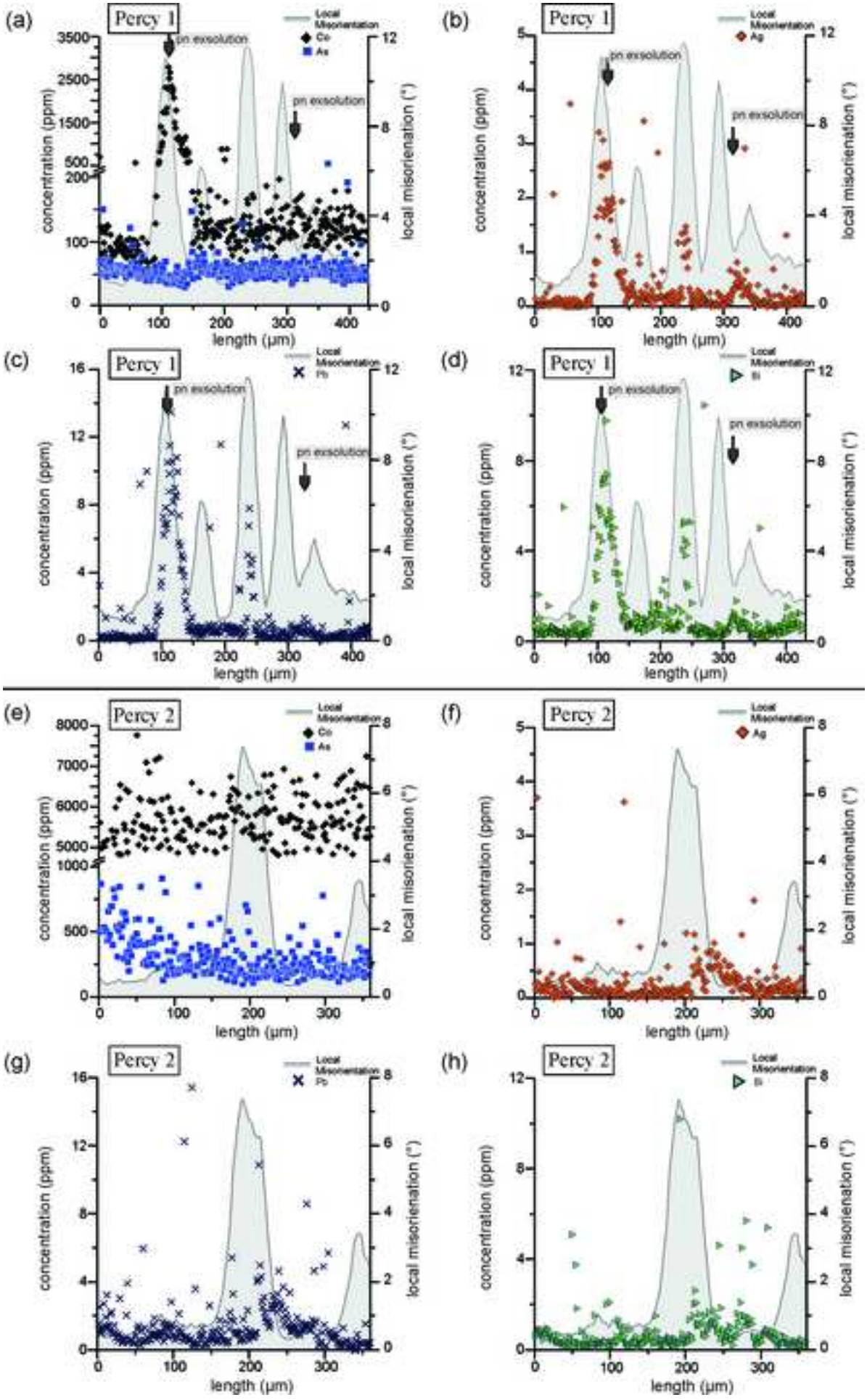

Figure 11

Click here to download high resolution image

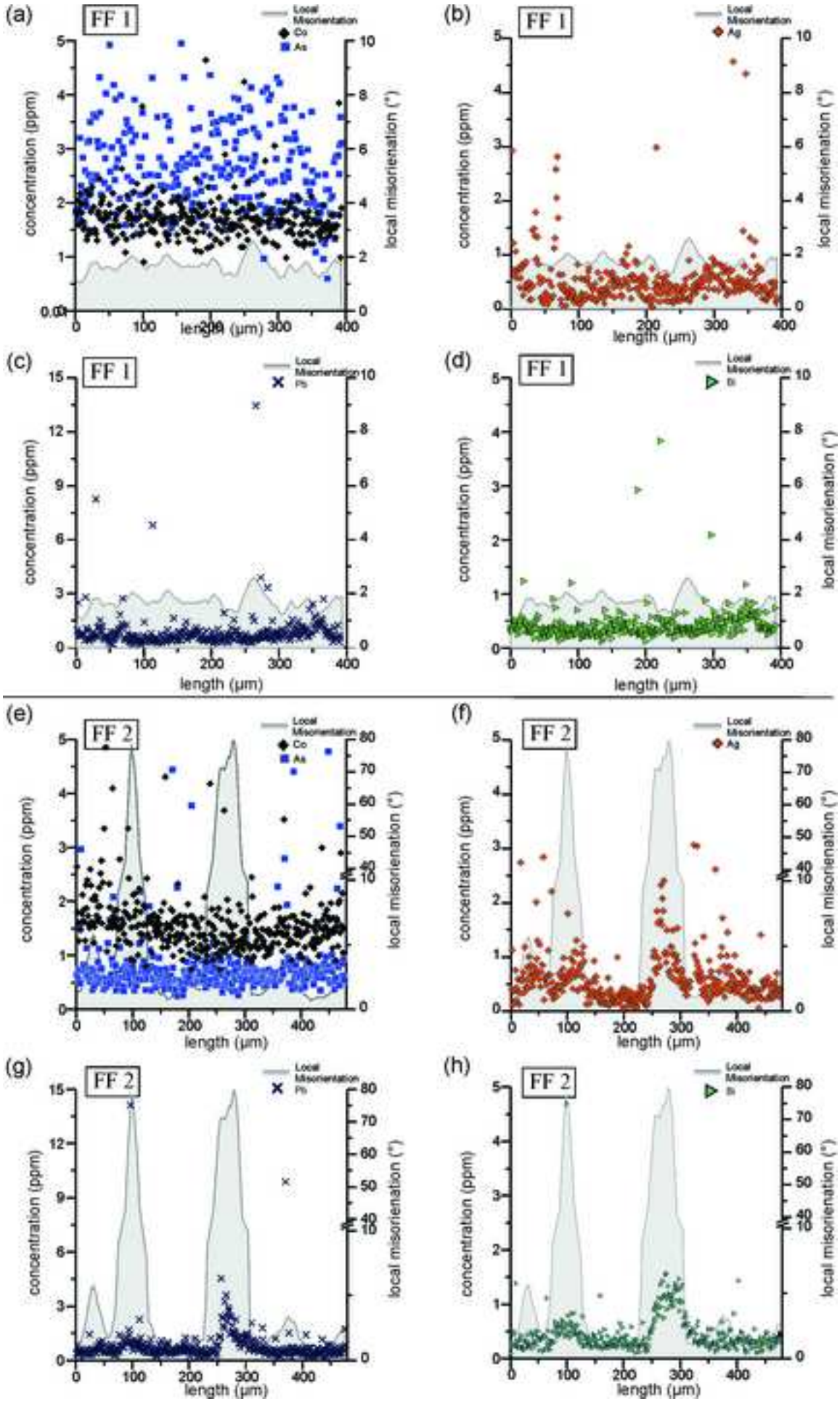

Figure 12

Click here to download high resolution image

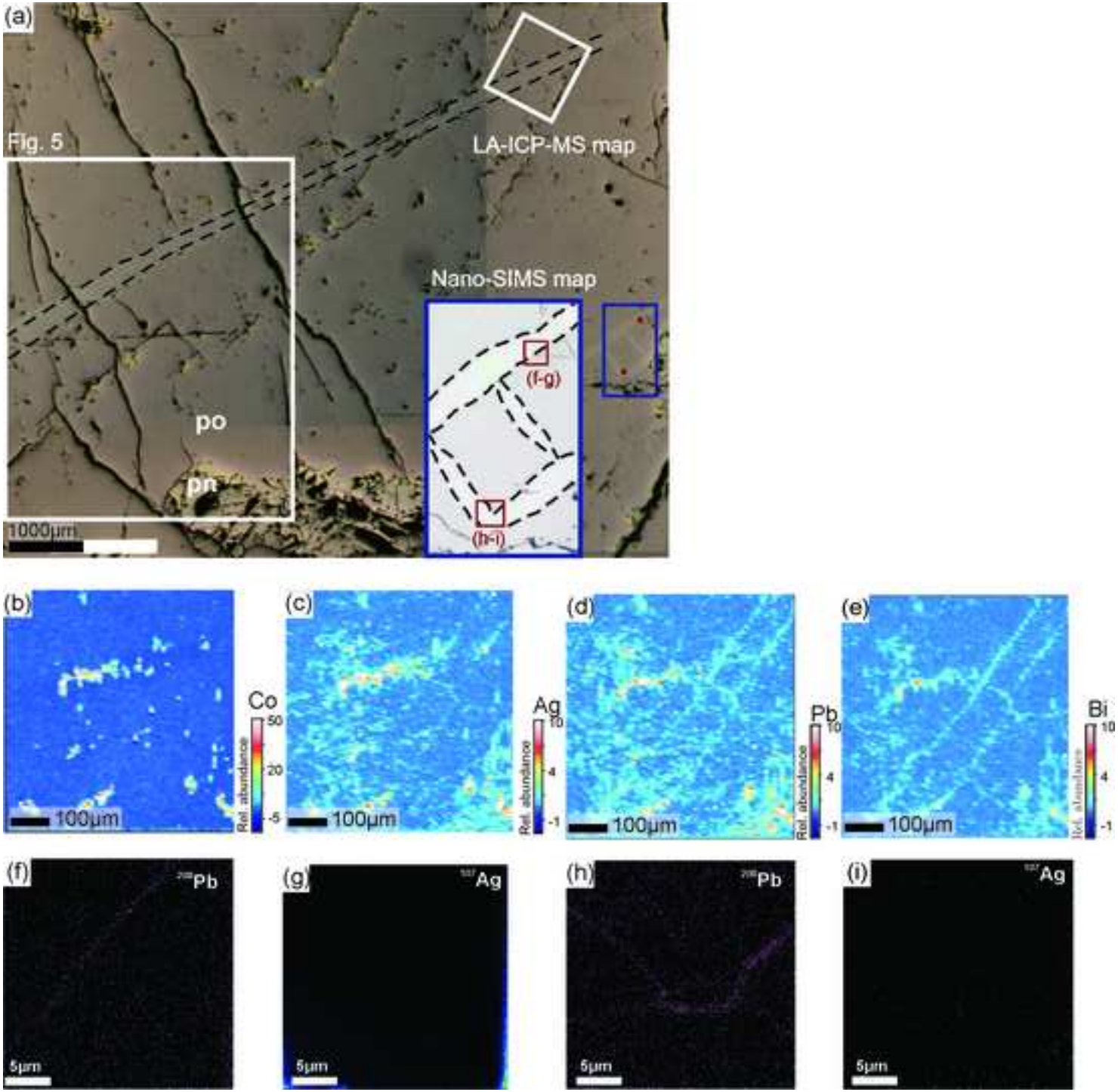

Figure 13

Click here to download high resolution image

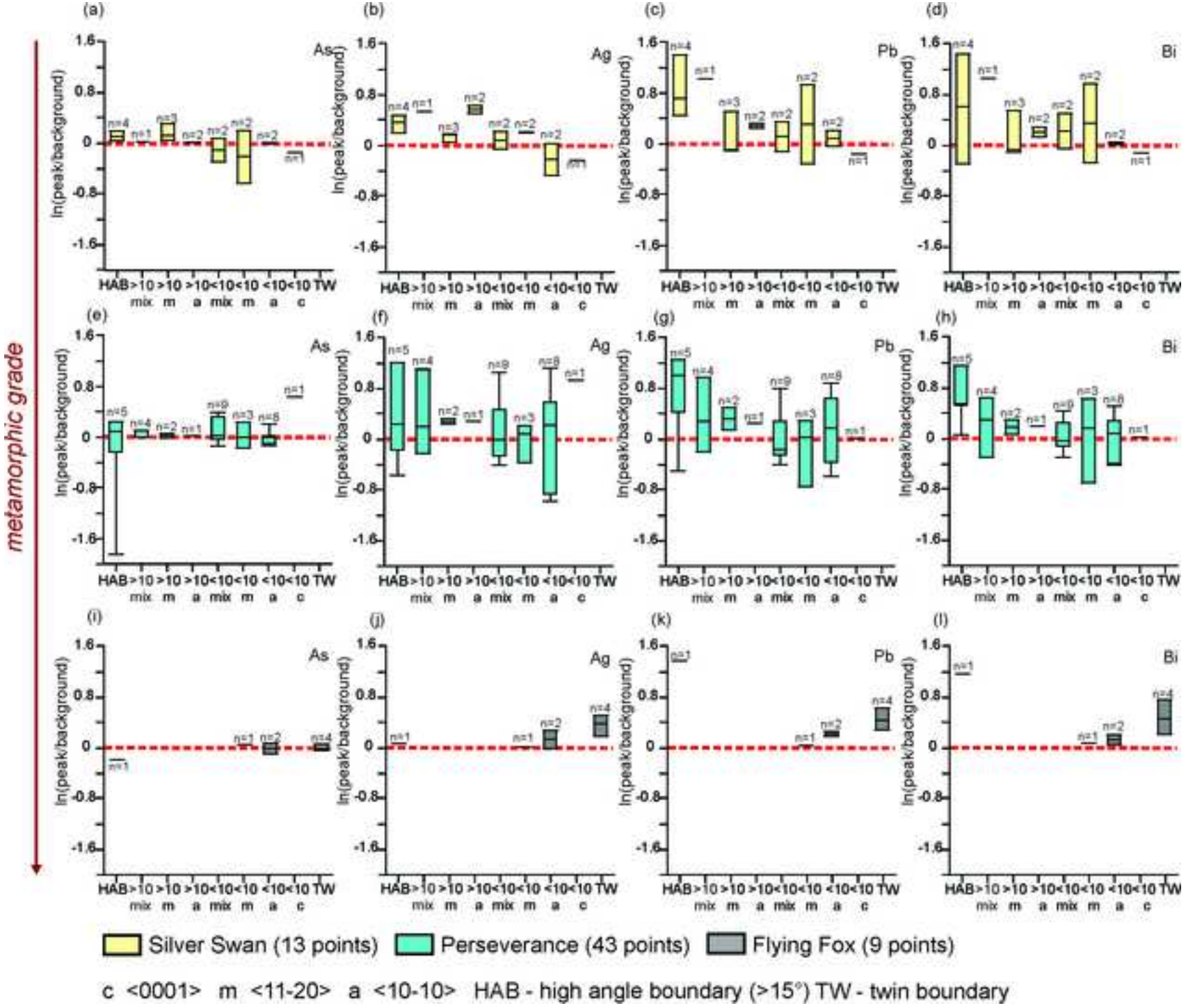

Figure 14

Click here to download high resolution image

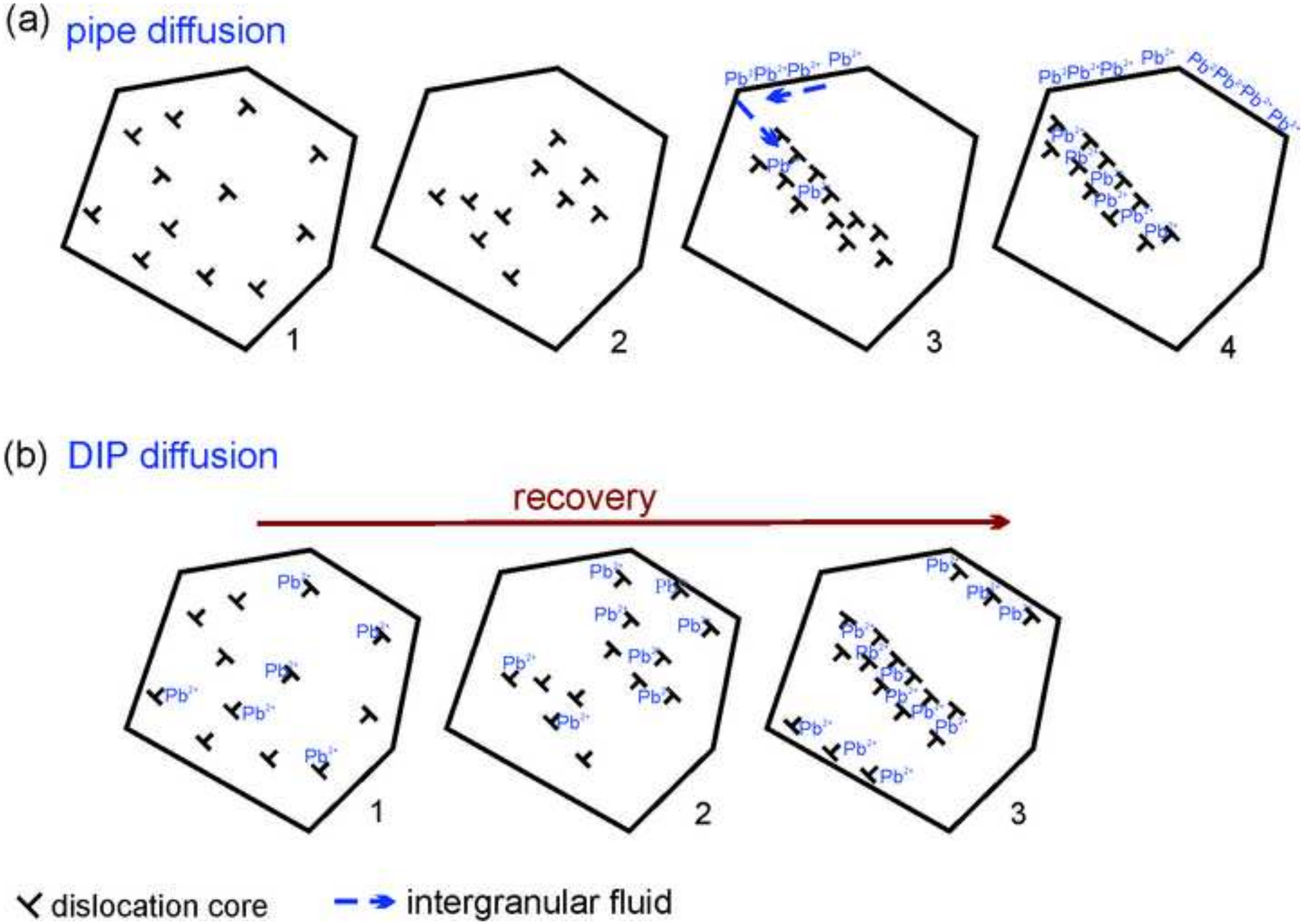

Table1

Click here to download Table: Table 1.pdf

Detection limits (ppm)		^{59}Co	^{75}As	^{107}Ag	^{105}Pd	^{108}Pd	^{189}Os	^{193}Ir	^{195}Pt	^{197}Au	^{208}Pb	^{209}Bi
Silver Swan	po	0.66	26.88	0.73	1.05	1.35	4.33	0.98	3.21	1.66	1.51	1.05
	py	0.27	10.79	0.32	0.91	0.41	0.00	0.44	1.52	0.67	0.95	0.37
Perseverance	po	0.17	43.43	0.63	0.07	0.00	0.54	0.10	0.58	0.35	0.69	0.04
	pn	5.31	91.84	0.46	0.07	3.20	0.54	0.11	0.67	0.22	0.73	0.07
Flying Fox	po	0.25	11.21	0.38	0.07	0.14	0.39	0.06	0.54	0.22	0.71	0.09

supplementary Table A1
Click here to download Table: Table A1.pdf

EBSD Settings	*samples*		
	Silver Swan	Perseverance	Flying Fox
EBSP collection time per frame	60		
Background (frames)	64		
EBSP noise reduction (frames)	4		
(Binning)	4 x 4		
(Grain)	low		
Hough detection	65		
Band detection (min/max)	8		
X steps	307	320	250
Y steps	217	300	334
Step size (µm)	5	10	10
MAD (pyrrhotite)	0.518	0.714	0.49
MAD (pentlandite)	0.629	0.486	n/a
MAD (pyrite)	0.481	n/a	0.621
Noise reduction "wildspike"	yes	yes	yes
n Naighbour zero solution extrapolation	5		
Kuwahara filter	3 x 3		

Table A 1 EBSD settings for the used in this study.

supplementary Table A2

Click here to download Table: Table A2.pdf

Standards		^{33}S	^{61}Ni	^{57}Fe	^{65}Cu	^{99}Ru	^{101}Ru	^{103}Rh	^{105}Pd	^{108}Pd	^{189}Os	^{193}Ir	^{195}Pt	^{197}Au	^{53}Cr	^{59}Co	^{66}Zn	^{75}As	^{82}Se	^{95}Mo	^{107}Ag	^{121}Sb	^{125}Te	^{208}Pb	^{209}Bi
		wt. %	wt. %	wt. %	wt. %	ppm	ppm	ppm	ppm	ppm	ppm	ppm	ppm	ppm	ppm	ppm	wt. %	ppm	ppm	ppm	ppm	ppm	ppm	ppm	ppm
NiSe*	Av	28.02	72.16	-	-	-	-	-	-	-	-	-	-	-	-	-	-	-	-	-	-	-	-	-	-
n# 16	StDev	0.259	1.676	-	-	-	-	-	-	-	-	-	-	-	-	-	-	-	-	-	-	-	-	-	-
	Accepted	28	72	-	-	-	-	-	-	-	-	-	-	-	-	-	-	-	-	-	-	-	-	-	-
	RSD %	0.92	2.33	-	-	-	-	-	-	-	-	-	-	-	-	-	-	-	-	-	-	-	-	-	-
Reference	in-house NiS bead used to estimate Ni interferance																								
Laflamme	Av	39.2	-	61.35	-	36.34	36.33	41.34	43.34	43.23	46.45	47.8	35.39	45.45	-	-	-	-	-	-	-	-	-	-	-
PO727*	StDev	0.50	-	2.05	-	1.57	1.53	2.11	2.28	2.17	2.74	2.74	2.58	2.99	-	-	-	-	-	-	-	-	-	-	-
n# 20	Accepted	39.09	-	61.07	-	36.5	36.5	41.6	43.4	43.4	46.7	48	35.5	45.8	-	-	-	-	-	-	-	-	-	-	-
	RSD %	1.27	-	3.36	-	4.29	4.19	5.07	5.24	5.00	5.88	5.71	7.27	6.52	-	-	-	-	-	-	-	-	-	-	-
Reference	certified reference material provided by the Memorial University of Newfoundland: syntetic FeS doped with PGE and Au																								
PS1*	Av	27.6	-	15.61	13.38	-	-	-	-	-	-	94.63	83.51	47.39	37.26	67.16	20.75	64.86	53.06	61.01	67.04	55.18	-	80.06	65.96
n# 16	StDev	0.06	-	3.57	1.98	-	-	-	-	-	-	0.81	0.28	1.35	1.24	1.88	0.17	2.36	0.80	0.88	1.12	0.93	-	1.26	0.69
	Accepted	276	-	15.6	13.4	-	-	-	-	-	-	94.6	83.5	47	37	67	20.74	65	53	61	67	55	-	80	66
	RSD %	0.02	-	22.91	14.80	-	-	-	-	-	-	0.86	0.33	2.87	3.35	2.81	0.80	3.64	1.50	1.44	1.67	1.69	-	1.57	1.05
Reference	provided by National Institute for Standards and Technology (NIST): ZuCuFeS pressed powder pellet doped trace elements																								
JB5**	Av	40.81	1.204	59.16	0.037	21.22	20.82	52.4	49.32	53.78	58.9	42.23	37.27	35.03	-	-	-	79.65	64.32	0.845	64.58	56.11	53.5	88.9	88.07
n# 20	StDev	0.59	0.42	5.27	0.03	2.24	2.12	12.23	8.01	4.88	8.52	5.16	4.07	2.67	-	-	-	24.89	9.15	0.15	6.61	4.96	14.71	12.59	10.49
	Accepted	40.47	1.049	57	208	21.68	21.68	61.4	65.2	65.2	42.58	40.21	39.9	35.9	-	-	-	79	47.27	0.23	53	61.3	44	71.5	76.1
	RSD %	1.46	39.68	9.25	0.01	10.31	9.79	19.91	12.28	7.48	20.02	12.83	10.20	7.43	-	-	-	31.51	19.36	65.92	12.47	8.08	33.43	17.61	13.78
Reference	provided by Prof. Brenan of the University of Toronto: syntetic FeS doped with chalcophile elements																								

* reference material used for callibration of the ICP-MS; ** reference material used as a monitor

Table A2 Estimation of LA-ICP-MS precision and accuracy based on analysis of FeS standards